

## Journal Pre-proofs

Research papers

Floodwater pathways in urban areas: a method to compute porosity fields for anisotropic subgrid models in differential form

Alessia Ferrari, Daniele P. Viero

PII: S0022-1694(20)30653-3

DOI: <https://doi.org/10.1016/j.jhydrol.2020.125193>

Reference: HYDROL 125193

To appear in: *Journal of Hydrology*

Received Date: 17 April 2020

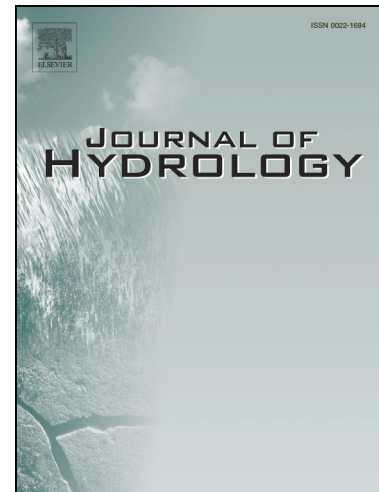
Revised Date: 10 June 2020

Accepted Date: 12 June 2020

Please cite this article as: Ferrari, A., Viero, D.P., Floodwater pathways in urban areas: a method to compute porosity fields for anisotropic subgrid models in differential form, *Journal of Hydrology* (2020), doi: <https://doi.org/10.1016/j.jhydrol.2020.125193>

This is a PDF file of an article that has undergone enhancements after acceptance, such as the addition of a cover page and metadata, and formatting for readability, but it is not yet the definitive version of record. This version will undergo additional copyediting, typesetting and review before it is published in its final form, but we are providing this version to give early visibility of the article. Please note that, during the production process, errors may be discovered which could affect the content, and all legal disclaimers that apply to the journal pertain.

© 2020 Published by Elsevier B.V.



# Floodwater pathways in urban areas: a method to compute porosity fields for anisotropic subgrid models in differential form

ALESSIA FERRARI, *PhD, Research Assistant, Department of Engineering and Architecture, University of Parma, Parco Area delle Scienze 181/A, 43124 Parma, Italy.*  
Email: [alessia.ferrari@unipr.it](mailto:alessia.ferrari@unipr.it)

DANIELE P. VIERO, *PhD, Assistant Professor, Department of Civil, Environmental and Architectural Engineering, University of Padova, via Loredan 20, 35131 Padova, Italy.*  
Email: [daniele.viero@unipd.it](mailto:daniele.viero@unipd.it)

## Abstract

In the framework of porosity models for large-scale urban floods, this work presents a method to compute the spatial distribution of the porosity parameters of complex urban areas by analyzing the footprints of buildings and obstacles. Precisely, an algorithm is described that estimates the four parameters required by the differential, dual-porosity formulation we recently presented. In this formulation, beside the common isotropic porosity accounting for the reduced storage volume due to buildings, a cell-based conveyance porosity is introduced in the momentum equations in tensor form to model anisotropic resistances and alterations in the flow direction due to presence of preferential pathways such as streets. A cell-averaged description of the spatial connectivity in the urban medium and of the preferential flow directions is the main ingredient for robust and mesh-independent estimates. To achieve this goal, the algorithm here presented automatically extracts the spatially distributed porosity fields of urban layouts relying only on geometrical information, thus avoiding additional calibration effort. The proposed method is described with the aid of schematic applications and then tested by simulating the flooding of real, complex urban areas using structured Cartesian grids. A Fortran implementation of the algorithm is made available for free download and use.

**Keywords:** Urban flood; porosity model; conveyance porosity; porous shallow water equations; spatially-distributed porosity field; anisotropic friction; structured grid.

## 1 Introduction

Urban flooding is recognized as a global challenge, exacerbated by the growth of megacities in flood-prone areas, by anthropogenic modifications of landscapes, and by climate change as well (Arnell and Gosling, 2016; Jongman et al., 2012; Tanoue et al., 2016; Viero et al., 2019).

The adoption of structural measures and complementary strategies to reduce the effects of floods (Kundzewicz et al., 2018; Mel et al., 2020), the achievement of increased resilience (Ferrari et al., 2020a; McClymont et al., 2020) and effective adaptation (Jongman, 2018; Muis et al., 2015; Radhakrishnan et al., 2018), all rely on the knowledge of the processes involved. The need of assessing flood hazard accurately entails the need of suitable modelling tools for large scale urban floods (Sanders, 2017; Sanders and Schubert, 2019; Vacondio et al., 2016; Wing et al., 2018).

In this view, subgrid porosity models for urban floods reproduce the effects of fine scale topography at a relatively coarse resolution, allowing physics-based, large-scale applications with limited need of computational resources. This kind of models has been the subject of ongoing research and of numerous applications (Braschi and Gallati, 1989; Bruwier et al., 2017; Chen et al., 2012a, 2012b; Costabile et al., 2020; Cozzolino et al., 2018; Defina, 2000; Defina et al., 1994; Ferrari et al., 2020b, 2017; Guinot, 2012; Guinot et al., 2017; Özgen et al., 2016; Sanders et al., 2008; Varra et al., 2020; Yu and Lane, 2011, 2006).

Here we draw the reader's attention to the dual-porosity model in differential form recently proposed by Viero (2019) and Ferrari et al. (2019), in which an isotropic porosity accounts for storage reduction due to the presence of buildings, and a directionally-dependent conveyance porosity is introduced in the momentum equations in tensor form to account for anisotropic resistances exerted by buildings and obstacles, and for the presence of preferential pathways. Both the storage and the conveyance porosities are defined at the cell-level. The model retains the mesh-independence typical of porosity models in differential form, and the natural inclusion of anisotropic effects related to alignment of buildings and obstacles typical of integral porosity models (Guinot et al., 2017; Sanders et al., 2008).

In previous contributions, the model by Ferrari et al. (2019) and Viero (2019) was only tested using uniform porosity parameters, averaged within the urban area, and assigned to all the computational cells therein. Actually, to our knowledge, porosity models in differential form were all used with uniform porosity so far (e.g., Cea and Vázquez-Cendón, 2010; Guinot, 2012; Guinot and Soares-Frazão, 2006; Soares-Frazao et al., 2008), with the only exception of the exploratory study by Soares-Frazão et al. (2018).

The use of uniform porosity parameters allows verifying the model skills in terms of global resistance exerted by a patch of urbanized area on the surrounding flow, yet it offers no chance of describing the spatial variability of the flow field within the urban area. Moreover, it has to be admitted that for increasingly larger urban areas, uniform porosity parameters become as difficult to estimate as meaningless from a physical point of view. That is to say, the modelling of real urban layouts is still an open challenge for porosity models in differential form.

Integral Porosity (IP) models (Guinot et al., 2017; Sanders et al., 2008) were introduced with the specific aim of accounting for the flow field variability within the urban fabric; yet, for how they are constructed, IP models suffer a marked sensitivity to the mesh design (Guinot, 2017a; Kim et al., 2015). Recently, Varra et al. (2020) argued that resorting to the differential approach does not prevent a model to supply meaningful information at the scale comparable to those of buildings (meters or tens of meters). Of course, porosity fields have to reflect the actual spatial variability of blocking features within the urban fabric.

With this in mind, in this work we present a method to infer the porosity parameters needed by the dual porosity model of Ferrari et al. (2019) and Viero (2019) automatically, for real and complex urban areas, making use of geometrical information only. This should assure model robustness and limit the need for successive model calibration.

Special care is devoted to the estimation of the conveyance porosity, for multiple reasons. Unlike in the Integral Porosity models, in which it is defined at the cell sides, conveyance porosity is here defined at the cell-level, i.e., it has to reflect the connectivity properties of the urban medium within the entire cell (Guinot, 2017a; Viero, 2019). This is both an opportunity and a challenge; the cell-based, spatially-averaged description of the spatial connectivity and of preferential flow directions is the main ingredient assuring robust and mesh-independent estimates; yet, conveyance porosity is actually directionally-dependent, thus entailing the need of recognising effective principal components (i.e., minimum and maximum conveyances) along with the associated directions, by only analysing the spatial distribution of building footprints. Importantly, the geometrically-based estimates must be effective in representing the real hydraulic behaviour of obstacles and preferential pathways within the cell. Thus, the method here presented computes the directionally-dependent conveyance porosity, its principal components and the associated directions, as well as storage porosity, from the building footprints of a given urban area on a cell-by-cell basis. A graphical method, based on the use of roseplots, is also proposed to preliminary check the effectiveness of the conveyance porosity estimates.

The paper is organized as follows. The key aspects of the dual-porosity formulation in differential form (Ferrari et al., 2019; Viero, 2019), together with the main features of the 2D accelerated shallow water model adopted in the work, are recalled in Sect. 2. The

method to automatically extract the porosity parameters from building footprints is described in Sect. 3 and made available in a permanent repository (see Appendix A). The method is then tested by simulating floods in real urban areas (Sect. 4). The discussion on the proposed procedure and some concluding remarks are finally outlined in Sect. 5.

## 2 Material and Methods

### 2.1 The dual porosity model in differential form

In the framework of urban flood modelling based on the Shallow Water Equations (SWEs) with porosity, the formulation recently presented in Ferrari et al. (2019) and Viero (2019) describes the effects exerted by buildings and obstacles by adopting an isotropic storage porosity and an anisotropic conveyance porosity, both defined at the cell level.

The isotropic porosity,  $\phi$ , accounts for the storage reduction due to the presence of buildings; it is evaluated for each computational cell as the ratio between the area free of obstacles and the total area (Figure 1a), as in single porosity (SP) and integral porosity (IP) models (Guinot and Soares-Frazão, 2006; Sanders et al., 2008).

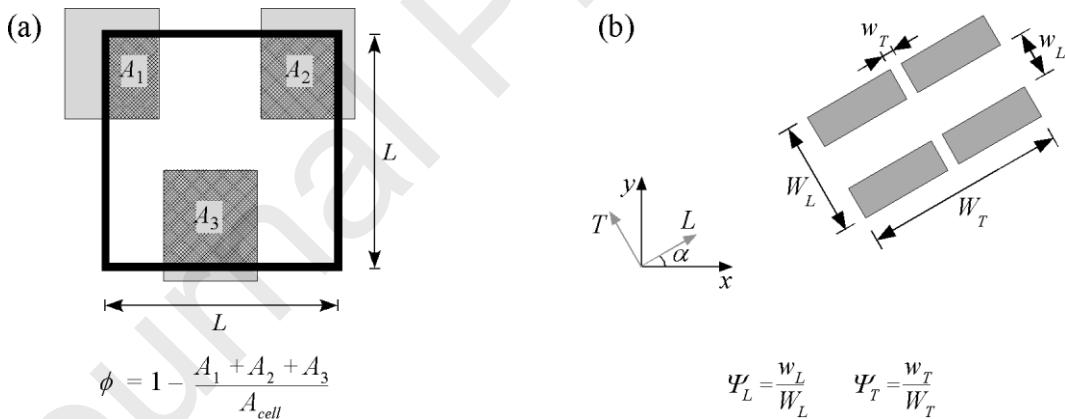


Figure 1. Definition of the four porosity parameters ( $\phi$ ,  $\Psi_L$ ,  $\Psi_T$ ,  $\alpha$ ) in the dual-porosity, anisotropic model by Ferrari et al. (2019) and Viero (2019): a) isotropic storage porosity,  $\phi$  (the thick black square is the computational cell with area  $A_{cell}$ ); b) anisotropic conveyance porosity defined by  $\Psi_L$ ,  $\Psi_T$ , and  $\alpha$ . Grey areas denote buildings.

On the other hand, the reduced conveyance, the alteration in the flow direction, and the presence of preferential flow pathways related to the alignment of buildings and obstacles, are accounted for by introducing in the momentum equations a directionally-dependent conveyance porosity in tensor form (Ferrari et al., 2019; Viero, 2019; Viero and Valipour, 2017). This conveyance porosity, which reflects the spatial distribution of obstacles and

preferential pathways *within* cell and not only at cell-edges, is the genuine novelty of the approach proposed by Ferrari et al. (2019) and Viero (2019). In previous SP models, in fact, preferential flow directions have been taken into account by introducing directional drag terms that essentially rely on model calibration (Velickovic et al., 2017), thus limiting the predictive power of the model. In the IP model (Sanders et al., 2008), and in the dual-IP model as well (Guinot et al., 2017), conveyance porosity is locally defined at the cell sides, thus making these models unusually sensitive to the mesh design (Guinot, 2017a).

In a one-dimensional (1D) framework, the conveyance porosity  $\Psi$  is analogous to the width ratio of a channel contraction (Defina and Viero, 2010), i.e., it is evaluated as the ratio between the width at the narrowest cross-section and the total width. In a two-dimensional (2D) framework (Figure 1b), the conveyance porosity assumes different values for different flow directions. It is then evaluated along the principal directions of maximum,  $L$ , and minimum,  $T$ , conveyance, resulting in the longitudinal,  $\Psi_L$ , and transverse,  $\Psi_T$ , conveyance parameters, which are supposed to be mutually orthogonal. Finally, the rotation angle between the  $L$ - $T$  frame and the  $x$ - $y$  model frame is expressed by the parameter  $\alpha$  (Figure 1b).

This dual-porosity approach has been implemented in two different 2D hydrodynamic models. Ferrari et al. (2019) described the implementation of the subgrid scheme in PARFLOOD, a GPU-enhanced Finite Volume model on Cartesian and multi-resolution grids (Vacondio et al., 2017, 2014); Viero (2019) described its implementation in 2DEF, a Finite Element, mixed Eulerian-Lagrangian model on staggered unstructured meshes (D'Alpaos et al., 2007; Defina, 2000; Viero et al., 2014, 2013). In the PARFLOOD and 2DEF models, the implementation of the dual-porosity model was slightly different: Viero (2019) used the conveyance porosity in tensor form to express both acceleration terms and friction losses; Ferrari et al. (2019) used the conveyance porosity for friction losses and kept the storage porosity for acceleration terms, to retain the general structure of classical Finite Volume schemes. To sum up, the implementation of the dual porosity scheme is more rigorous in Viero (2019), but the 2DEF model is neither suitable to deal with shock waves, nor with rapidly varying flows; on the other hand, although accounting for anisotropic effects only through friction losses, the porous version of PARFLOOD described in Ferrari et al. (2019) is shock-capturing and suitable for subcritical, supercritical, and rapidly-varying flows. Nevertheless, both the schemes were shown to provide reasonably good results in their respective field of applications. In the present work, the effectiveness of the porosity parameters estimated from building footprints with the method described in the following Sect. 3, is tested using the model by Ferrari et al. (2019), whose main features are briefly recalled in the following section.

## 2.2 The porous version of the PARFLOOD numerical model

In the PARFLOOD model, according to Ferrari et al. (2019), the four parameters  $\phi$ ,  $\Psi_L$ ,  $\Psi_T$ , and  $\alpha$ , are introduced in the system of 2D-SWEs written in integral form (Toro, 2001):

$$\frac{d}{dt} \int_A \mathbf{U} dA + \int_C \mathbf{H} \cdot \mathbf{n} dC = \int_A (\mathbf{S}_0 + \mathbf{S}_f + \mathbf{S}_p) dA \quad (1)$$

where  $A$  and  $C$  are the area and the boundary of the integration element, respectively,  $\mathbf{n}$  is the outward unit vector normal to  $C$ . The vector of the conserved variables,  $\mathbf{U}$ , and the tensor of fluxes in the  $x$  and  $y$  directions,  $\mathbf{H} = (\mathbf{F}, \mathbf{G})$ , are defined as:

$$\mathbf{U} = \begin{bmatrix} \eta \\ uh \\ vh \end{bmatrix} \quad \mathbf{F} = \begin{bmatrix} uh \\ u^2h + \frac{1}{2}g(\eta^2 - 2\eta z) \\ uvh \end{bmatrix} \quad \mathbf{G} = \begin{bmatrix} vh \\ uvh \\ v^2h + \frac{1}{2}g(\eta^2 - 2\eta z) \end{bmatrix} \quad (2)$$

with  $h$  the water depth,  $\eta$  the water surface elevation,  $z$  the bottom elevation,  $g$  the gravitational acceleration,  $u$  and  $v$  the velocity components in the  $x$  and  $y$  directions, respectively.

The bed slope source term,  $\mathbf{S}_0$ , and the porosity-related non-conservative product,  $\mathbf{S}_p$ , are defined as:

$$\mathbf{S}_0 = \begin{bmatrix} 0 \\ -g\eta \frac{\partial z}{\partial x} \\ \frac{\partial z}{\partial y} \\ -g\eta \frac{\partial z}{\partial y} \end{bmatrix} \quad \mathbf{S}_p = \begin{bmatrix} -\frac{h}{\phi} \left( u \frac{\partial \phi}{\partial x} + v \frac{\partial \phi}{\partial y} \right) \\ -\frac{uh}{\phi} \left( u \frac{\partial \phi}{\partial x} + v \frac{\partial \phi}{\partial y} \right) \\ -\frac{vh}{\phi} \left( u \frac{\partial \phi}{\partial x} + v \frac{\partial \phi}{\partial y} \right) \end{bmatrix} \quad (3)$$

Finally, the friction source term,  $\mathbf{S}_f$ , is obtained by first projecting the flow velocity on the  $L$ - $T$  frame and then projecting friction components back to the  $x$ - $y$  frame, thus accounting for anisotropic conveyance porosity as follows (Ferrari et al., 2019):

$$\mathbf{S}_f = \begin{bmatrix} 0 \\ -gh \frac{n^2 u_{eL} \sqrt{u_{eL}^2 + u_{eT}^2}}{h^{4/3}} \cos \alpha + gh \frac{n^2 u_{eT} \sqrt{u_{eL}^2 + u_{eT}^2}}{h^{4/3}} \sin \alpha \\ -gh \frac{n^2 u_{eL} \sqrt{u_{eL}^2 + u_{eT}^2}}{h^{4/3}} \sin \alpha - gh \frac{n^2 u_{eT} \sqrt{u_{eL}^2 + u_{eT}^2}}{h^{4/3}} \cos \alpha \end{bmatrix} \quad (4)$$

where  $n$  is the Manning coefficient,  $u_{eL} = u_L \phi / \Psi_L$  and  $u_{eT} = u_T \phi / \Psi_T$  are the effective velocity components along the  $L$  and  $T$  directions, respectively.

As pointed out in Ferrari et al. (2019), the formulation guarantees the well-balancing between fluxes and source terms (Liang and Borthwick, 2009), and preserves the  $C$ -property also in presence of wet-dry fronts, regardless the slope source term discretization (Liang and Marche, 2009). The numerical fluxes in Eq. (2) are computed at the cell interfaces adopting the HLLC approximate Riemann solver (Toro, 2001). A robust treatment of non-physical velocities, which may develop at wet-dry fronts, is ensured, with a zero-mass error, by adopting the flux correction of Kurganov and Petrova (2007).

The numerical scheme achieves both first and second order of accuracy. This last approximation in space is ensured by reconstructing the conserved variables at the cell edges by means of the linear Monotone Upwind Schemes for Scalar Conservation Laws (MUSCL) with *minmod* limiter (Toro, 1999). The conserved variables are updated at each time step according to the second order Runge-Kutta method, providing a second-order accuracy in time.

The set of partial differential equations can be solved on two different structured grids, both Cartesian (Vacondio et al., 2014) and multi-resolution Block Uniform Quadtree (BUQ, Vacondio et al., 2017). Given that the dual-porosity approach is not over-sensitive to the mesh design, it can be safely implemented on structured grids, which cannot be adapted to meet the strict requirements of proper mesh design needed by, e.g., IP models (Guinot, 2017a).

With reference to the implementation technique, the explicit finite volume scheme is written in CUDA/C++ architecture that exploits parallel computation offered by NVIDIA™ Graphic Processing Units (GPUs), thus significantly reducing the computational time.

### 3 A procedure to infer porosity parameters from building footprints

#### 3.1 Basic principles

In simulating urban floods with porosity models, the adoption of coarse grids entails an unavoidable loss of detail in the representation of the flow field within a urban area, with respect to the use of fine grids that resolve buildings explicitly. This loss of detail becomes substantial when models are used with uniform porosity distributions within an entire urban district, which is the common practice for porosity models in differential form (e.g., Cea and Vázquez-Cendón, 2010; Guinot, 2012; Guinot and Soares-Frazão, 2006; Soares-Frazao et al., 2008).

To find a reasonable trade-off between computational effort and spatial resolution of the flow field description, first, the grid resolution has to be adequate to the length-scale of the problem (i.e., comparable to the width of streets and buildings), and second, the porosity parameters must reflect the spatial distribution of obstacles and preferential pathways *within* the urban fabric. While the first requirement is relatively easy to meet, the second one is actually an open challenge.

This last issue is here addressed in the framework of the dual-porosity model in differential form described in Sect. 2.1. The four porosity parameters required by the model are supposed to vary inside the built-up area, so as to account for the spatial distribution of



obstacles and preferential flow paths within the urban area. Accordingly, porosity parameters are estimated on a genuine cell-by-cell basis. This is expected to improve the description of the effects exerted by buildings on the flow field, both close to and inside the urban area, at a spatial scale comparable to that of the (relatively) coarse grid. The same basic idea has been theoretically supported by Varra et al. (2020), and has been tested by Soares-Frazão et al. (2018) in the framework of SP porosity models (plus drag terms in tensor form), highlighting the benefits of accounting for distributed porosity based on the actual layout of buildings and streets.

The present method for estimating porosity distributions in real urbanized areas is designed to fulfil some basic principles: *i*) the spatial distribution of the porosity parameters should only rely on geometrical information, so as to reduce the successive need of model calibration (Arrault et al., 2016), *ii*) the estimation of porosity parameters should be inferred automatically, so as to allow straightforward large-scale model applications, and *iii*) the procedure should be intuitive and controlled by few parameters of clear physical meaning, so as to promote easy and trustful use by practitioners.

### 3.2 Spatially-distributed porosity fields from urban geometry

Given a relatively coarse computational grid covering a built-up area, the porosity parameters are evaluated by applying the procedure described in the following to each computational cell.

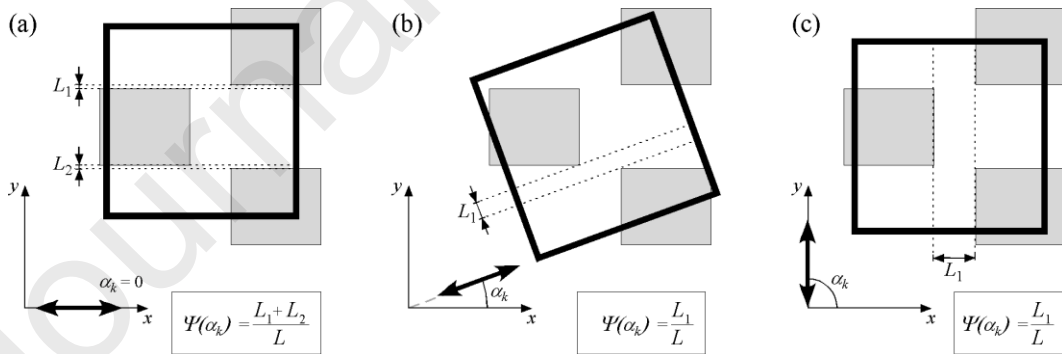


Figure 2. For a single computational cell with side length  $L$  (thick black square), the sketch depicts the general procedure used to evaluate the conveyance porosity for three given mean flow directions (identified by the thick double-headed arrow), namely  $\alpha_k = 0^\circ$  (a),  $\alpha_k = 20^\circ$  (b), and  $\alpha_k = 90^\circ$  (c). Grey areas denote buildings.

In extracting the porosity parameters from geometrical information, the computation of the storage porosity,  $\phi$ , is straightforward (Figure 1a), whereas estimating conveyance porosity effectively is far more complicated, as it requires the joint estimation of the principal components and of the associated angles. Indeed, the conveyance porosity is

directionally-dependent, and the angles that define the principal directions are not known a-priori.

In general, for a hypothetical mean flow direction at an angle  $\alpha_k$  to the  $x$  axis (double-headed arrow in Figure 2), the conveyance porosity  $\Psi(\alpha_k)$  should be estimated as the width ratio of the narrowest cross-section, in analogy to the definition of Figure 1b. Then, considering that the function  $\Psi(\alpha_k)$  is periodic with period  $\pi$ , i.e.,  $\Psi(\alpha_k) = \Psi(\alpha_k + \pi)$ , the function  $\Psi(\alpha_k)$  should be characterized for (discrete values of)  $\alpha_k$  in the range  $[0; \pi[$ . Finally, once known the behaviour of  $\Psi(\alpha_k)$ , a proper criterion should allow identifying the principal components of the conveyance porosity,  $\Psi_L$  and  $\Psi_T$ , along with the angle  $\alpha$  that identifies the direction of maximum conveyance  $\Psi_L$  (Figure 1b).

The proposed approach is a step forward with respect to Bruwier et al. (2017), who determined the conveyance porosities by evaluating the minimum areas across a coarse cell only in the  $x$  and  $y$  directions.

The procedure for the computation of the conveyance porosity principal components is implemented in two different versions, denoted as segment-based and strip-based methods, as described in the following. The code, implemented in Fortran language, is made available as supplementary material (see Appendix A).

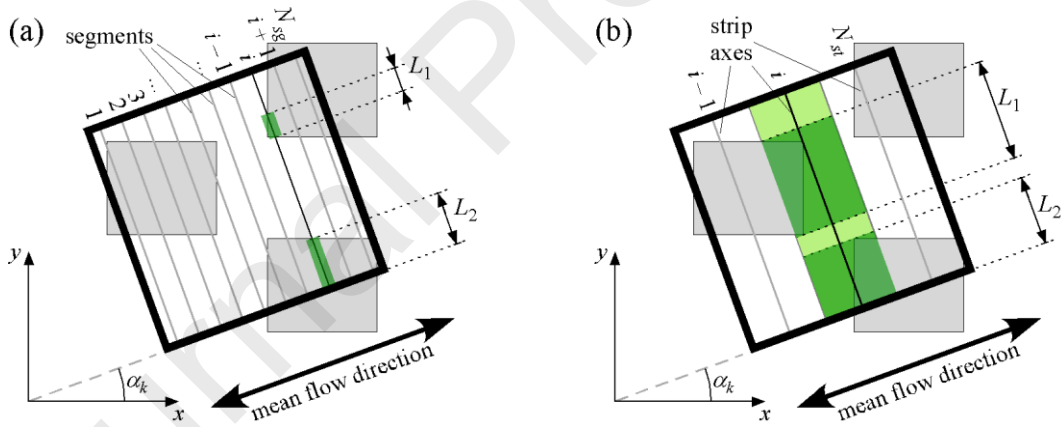


Figure 3. Segment-based (a) and strip-based (b) methods for computing the conveyance porosity for a mean flow direction  $\alpha_k$ . The thick black square is a computational cell with side length  $L$ ; the grey areas denote buildings.  $L_1$  and  $L_2$  denote the occupied parts of the  $i$ -th segment or strip (highlighted in dark green).

### 3.2.1 Anisotropic conveyance porosity: segment-based method

The first version of the algorithm that computes the porosity parameters is denoted as segment-based method (Figure 3a). It has to be applied to each cell of the computational grid, and consists in the following steps:

1. identify the buildings and obstacles whose footprint intersects the cell;

2. compute the storage porosity,  $\phi$ , which is the complement to unity of the fraction of cell area occupied by buildings (Figure 1a), using any polygons intersection routine;
3. span the sampling directions,  $\alpha_k$ , in the interval  $[0; \pi[$  as in Figure 2. Given a number of directions to be considered,  $N_\alpha$ , the angular spacing (in degrees) is  $\Delta\alpha = 180^\circ / N_\alpha$ . The  $k$ -th sampling direction is  $\alpha_k = (k - 1) \cdot \Delta\alpha$ , with  $k \in [1, N_\alpha]$ . A recommended value for  $\Delta\alpha$  is  $1^\circ$ ;
4. segment sampling. The cell is temporarily rotated by  $\alpha_k$  and sampled by considering  $N_{sg}$  equispaced segments (denoted with index  $i$ ), with spacing  $d_{sg} = L / N_{sg}$  (Figure 3a);
5. evaluate the free length for each of the  $N_{sg}$  segments. For each segment  $i$ , once detected the  $N_j$  parts that overlap the building footprints ( $L_1$  and  $L_2$  in Figure 3a), the total free length is computed as  $L_i^{free} = L - \sum_{j=1}^{N_j} L_j$ ;
6. evaluate the conveyance porosity in the  $\alpha_k$  direction as the ratio of minimum free length to segment length,  $\Psi_{\alpha_k} = \min_i (L_i^{free}) / L$ . This is a simple estimate of the width ratio of the narrowest cross-section for the given mean flow direction;
7. find the angle  $\alpha$  for which the (reciprocally orthogonal) principal components of the conveyance porosity  $\Psi_L$  and  $\Psi_T$  are closest to the maximum and minimum values among the  $N_\alpha$  values of the function  $\Psi(\alpha_k)$ , respectively. The goal is achieved by finding  $\alpha_k$  such that the product  $P_\Psi = \Psi_{\alpha_k} \cdot (1 - \Psi_{\alpha_k + \pi/2})$  is maximum, and setting  $\alpha = \alpha_k$ . Indeed,  $P_\Psi$  attains a maximum when  $\Psi$  is large along  $\alpha_k$ , and small in the orthogonal direction,  $\alpha_k + \pi/2$  (see Figure 4f for an example);
8. determine  $\Psi_L$  and  $\Psi_T$ . Considering that the minimum and maximum values of  $\Psi(\alpha_k)$  are not always orthogonal to each other, a trade-off is needed. The  $L$  direction should coincide with that of maximum conveyance,  $\alpha$ , to preserve the flux alignment in preferential pathways (e.g., streets), and  $\Psi_T$  should be taken as the minimum value of conveyance to represent blocking features correctly. Accordingly, the conveyance parameters are assumed as  $\Psi_L = \Psi(\alpha)$  and  $\Psi_T = \min[\Psi(\alpha_k)]$ .

### 3.2.2 Anisotropic conveyance porosity: strip-based method

The second version of the algorithm is denoted as strip-based method (Figure 3b). Only points 4 and 5 differ from the segment-based method described above:

4. strip slicing. The cell is temporarily rotated by  $\alpha_k$  and sliced in  $N_{st}$  strips (denoted with index  $i$ ). Each strip has width  $d_{st} = L / N_{st}$  (Figure 3b, in which  $N_{st} = 3$  and  $d_{st} = L/3$ );
5. evaluate the free length for each of the  $N_{st}$  strips. For each  $i$ -th strip, once found the  $N_j$  projections on the strip axis of each (part of) building that overlaps the strip ( $L_1$  and  $L_2$

in Figure 3b), the total length of the strip axis, free of any building projection, is evaluated as  $L_i^{free} = L - \sum_{j=1}^{N_j} L_j$ .

### 3.2.3 Graphical representation of the conveyance porosity

To judge the strengths and weaknesses of the above methods, the first step consists in visualizing the algorithm results in terms of directionally dependent conveyance porosity,  $\Psi(\alpha_k)$ . To reach the goal, in the figures hereinafter and in the supplementary data (see Appendix A), the (coarse) grid is superposed to the building footprints and, for each cell, the roseplot of  $\Psi(\alpha_k)$  is plotted. Considering that  $\Psi(\alpha_k)$  ranges in the interval  $[0, 1]$ , for each of the  $N_\alpha$  sampling directions, the coordinates of the roseplot line vertexes ( $x_{RP}$ ,  $y_{RP}$ ) are obtained as

$$\begin{aligned} x_{RP} &= x_C + 0.4 \cdot L \cdot \Psi(\alpha_k) \cdot \cos(\alpha_k) \\ y_{RP} &= y_C + 0.4 \cdot L \cdot \Psi(\alpha_k) \cdot \sin(\alpha_k) \end{aligned} \quad (5)$$

where  $(x_C, y_C)$  is the cell center, and 0.4 is a coefficient that determines the size of the roseplot with respect to the grid size,  $L$ . For each cell, two diametral segments are plotted that denote the  $L$  (blue) and  $T$  (red) directions of maximum and minimum conveyance, as determined according to points 7 and 8 in Sect. 3.2.1.

### 3.3 Considerations on the segment-based and strip-based methods

This section aims at discussing the pros and cons of the two methods previously described.

The segment-based method is the plainest way to face the problem of conveyance porosity evaluation, but it is subject to some limitations. A very small segment spacing,  $d_{sg}$ , is required to sample the cell in order to capture the possible presence of linear blocking features as thin walls (Hodges, 2015). This entails a large number of segments to be analyzed, which requires a significant computational effort (even if it is performed only once before running the simulation). Most importantly, the free length of each segment,  $L_i^{free}$ , is estimated regardless of what happens upstream and downstream of the segment itself, seldom leading to inconsistencies. This is shown with some examples.

In Figure 4, a slender building (or a linear blocking feature) is sampled through segments (a) and strips (d), for the hypothetical flow direction  $\alpha_k = 90^\circ$ . The roseplots of  $\Psi(\alpha_k)$  are obtained by analyzing all directions in the range  $[0, \pi[$ . Panels (c) and (f) show the trend of  $\Psi(\alpha_k)$  (green lines), which is then translated by  $\pi/2$  (grey lines), to obtain its complement to one (grey dashed line) and, in turn, the product  $P_\Psi(\alpha_k)$  (black dotted line).

The longitudinal ( $L$ ) direction (blue lines in b,c,e,f) is the one that maximizes the product  $P_\psi$ , and the transverse ( $T$ ) direction (red lines in b,c,e,f) is assumed as orthogonal to  $L$ ; this is the criterion chosen to determine the (most reliable) principal components for conveyance  $\Psi$  according to point 7 in Sect. 3.2.1.

In Figure 4, while the segment-based method (a) is unable to recognize the whole width of the obstacle (the green segments as far shorter than the total building width), the strip-based method succeeds since the dark green portion of the strip in (d) is as wide as the obstacle. The segment-derived roseplot in (b) shows similar values of  $\Psi(\alpha_k)$  in the north-south and in the east-west directions; as a consequence, the criterion based on the product  $P_\psi$  is unable to recognize orthogonal principal directions of maximum and minimum conveyance properly (c). The strip-based roseplot (e) shows a significantly lower conveyance in the north-south direction and more realistic results also for the entire range of directions; this allows detecting the principal directions correctly.

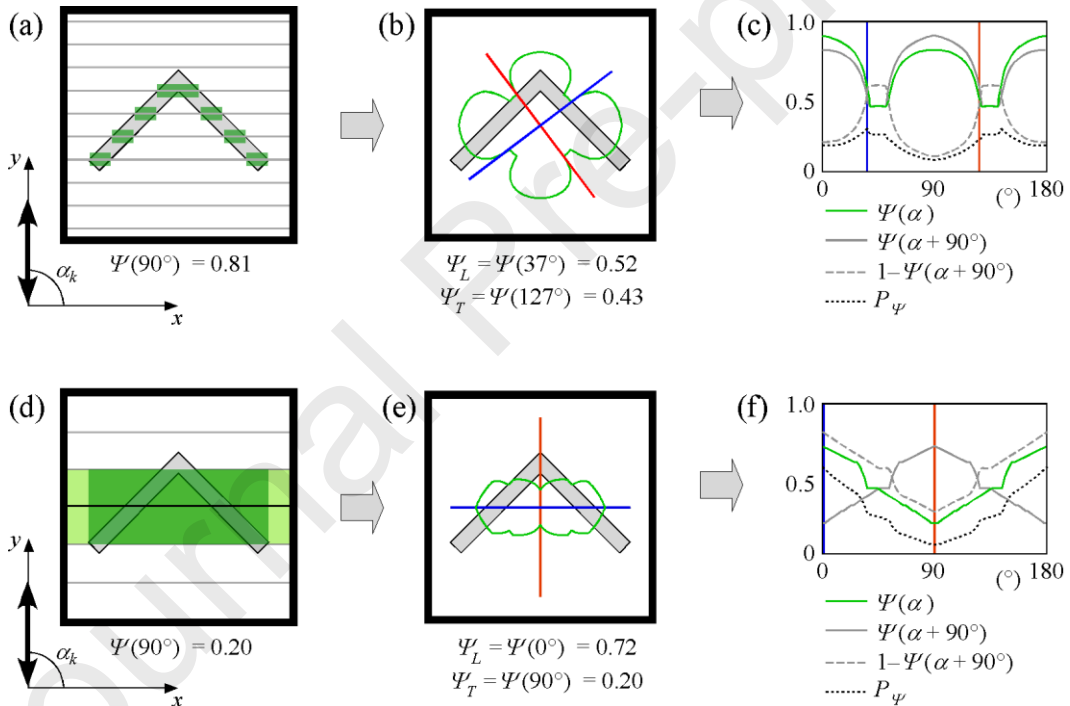


Figure 4. Example of segment-based (upper row) and strip-based (lower row) methods applied to a computational cell (thick black square) with a single slender building (grey area). Conveyance porosity for a mean flow direction  $\alpha_k = 90^\circ$  (a, d) and for the whole range of flow directions,  $\alpha_k \in [0; \pi]$  (b, e). Criterion for detecting the principal directions according to point 7 in Sect. 3.2.1 (c, f). The principal directions of maximum (blue) and minimum (red) conveyance are shown in panels (b,c,e,f).

The comparison of panels (c) and (f) in Figure 4 suggests that the criterion to determine the principal components, described at point 7 in Sect. 3.2.1, works well when  $\Psi(\alpha_k)$  shows (nearly) orthogonal maxima and minima, otherwise it fails in determining the direction of

minimum conveyance (but not the value of minimum conveyance,  $\Psi_T$ , which is chosen regardless of the actual value of  $\Psi$  in the  $T$  direction, according to point 8 in Sect. 3.2.1).

In Figure 5, the segment- and strip-based methods are applied to the checkerboard building arrangement of the Toce experiment (Testa et al., 2007). To obtain accurate results in the same urban layout using a coarse grid, Ferrari et al. (2019) highlighted the need of using lower values of conveyance porosity than the free length computed for a single row of buildings. Indeed, the staggered arrangement of buildings imposes severe, successive deviations to the flow, thus increasing the resistances with respect to the case of aligned buildings. For this reason, the conveyance porosity computed accounting for a single row of buildings is far greater than the effective one.

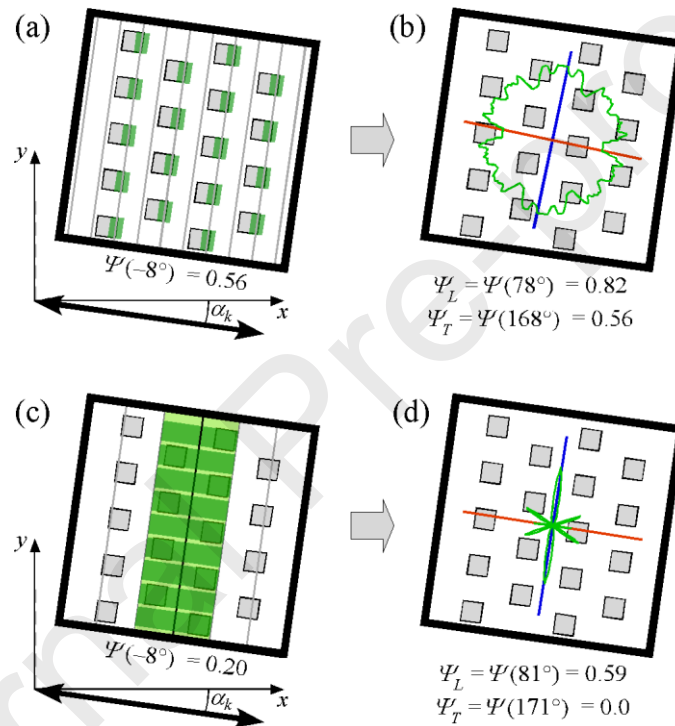


Figure 5. Example of segment-based (upper row) and strip-based (lower row) methods applied to a computational cell (thick black square) with the checkerboard arrangement of buildings (grey area) of the Toce experiment. Conveyance porosity for a mean flow direction  $\alpha_k = -8^\circ$  (a, c) and for the whole range of flow directions,  $\alpha_k \in [0; \pi[$  (b, d). The principal directions of maximum (blue) and minimum (red) conveyance are shown in panels (b) and (d).

Although the segment-based method is expected to work properly when the grid size is comparable to (or smaller than) the size of buildings, when using coarser grids as in Figure 5a, the segment-based sampling is unable to capture the tortuosity of floodwater pathways within the cell, thus overestimating the real conveyance. The strip-based method is expected to perform similarly well to the segment-based method for finer grids, and significantly better in case of coarser grids (as in the case of Figure 5c). In the considered

direction, the strip-based estimate of conveyance porosity accounts for the staggered arrangement of buildings, i.e., for the tortuosity of pathways within the cell. The obtained value corresponds to the theoretical one,  $\Psi(-8^\circ) = 0.2$  (buildings are 0.15 m wide and  $L = 1.7$  m in this case).

To sum up, the strip-based method improves the estimation of the conveyance porosity by considering all the blocking features that overlap a strip orthogonal to the assumed flow direction. By increasing the strip width, information is added that concerns the presence of obstacles both upstream and downstream. Accordingly, a tortuous path is given a lower conveyance porosity than a straight path.

It is interesting to note that the strip-based method reduces to the segment-based method in the limit  $d_{st} \rightarrow 0$ , with  $d_{st}$  the strip width, thus implying that the segment-based method is actually a special case of the more general strip-based method.

In view of giving some operating instructions on the application of the strip-based method, the strip width has to be chosen as large as possible (i.e.,  $d_{st} = L$ ) in order to recognize the real direction of preferential pathways (e.g., streets) correctly, and also to reflect the tortuosity of floodwater pathways within each single cell. On the other hand, when very coarse grids are used to model dense urban layouts with irregularly arranged obstacles, the adoption of excessively wide strips may result in a significant underestimation of the conveyance porosity. Simply speaking, one can obtain  $\Psi_L = \Psi_T = 0$ , meaning that the flow is inhibited in all directions, also when obstacle interspaces are well interconnected. Accordingly, to reflect the connectivity of the urban medium yet avoiding misrepresentations, the strip width should be taken larger than the typical length scale of the urban layout, although being careful of not exceeding it too much.

Finally, focusing on the computational efforts required by the two methods, the strip-based method is generally faster as the number of strips,  $N_{st}$ , is typically much smaller than the number of segments,  $N_{sg}$ , implying that the number of line/polygon intersections to be computed is largely lower for the strip-based method. Nonetheless, it is worth noting that the porosity parameters are evaluated for each cell of the (coarse) grid only once, in a pre-processing step. The computation of the spatially distributed porosity parameters, for the finest meshes of the test cases shown in Sect. 4, is performed in a few minutes, and does not affect the simulation runtime. The resulting parameters are kept constant during the simulation, thus assuming that both storage and conveyance porosities are not depth-dependent (Bruwier et al., 2017; Guinot et al., 2018; Li and Hodges, 2019; Özgen et al., 2016, 2015; Rong et al., 2020).

## 4 Results

The segment- and strip-based methods presented in Sect. 3 are tested by simulating the flooding in a laboratory experiment (the Toce case study, Testa et al., 2007) and in two real urban districts. The laboratory experiment with staggered obstacles is chosen because previous applications of the porosity model (with a uniform porosity distribution) required particular values of porosity parameters, a need that makes not obvious the successful application of the present algorithm. Then, since the main novelty of this work is to compute the porosity parameters in real urban layouts, two districts in Northern Italy are chosen as benchmarks, which are representative of complex urban fabrics with irregular shaped buildings and streets, courtyards, gardens walls, etc.

In all the tests, the spatial distribution of the four porosity parameters is extracted geometrically using the two above methods, and the PARFLOOD model is used to solve the porous 2D-SWEs with anisotropic friction (see Sect. 2.2). The model results are compared against reference, refined solutions, obtained by solving the classical 2D-SWEs (again with the PARFLOOD model) on fine grids in which buildings and obstacles are explicitly resolved (“building hole” method, Schubert and Sanders, 2012). All the simulations were run on a NVIDIA® Tesla® P100 GPU.

The model sensitivity to the bottom roughness and to the inflow boundary conditions was already addressed in Ferrari et al. (2019). Hence, in this work only the sensitivity of the porosity model to the mesh size and to the parameters controlling the computation of conveyance is tested. It is well known that the size of the (coarse) grid cells affects the accuracy of the numerical solution in terms of flow depth and velocity (Sanders and Schubert, 2019); more importantly, in this case the porosity fields are expected to change dramatically with the resolution of the (coarse) grid. This is because the number and the position of buildings and obstacles within a cell strongly depend on its size and location. The goal is to demonstrate that the change of grid resolution and the contextual change in the porosity fields lead to similar results, and that these results tend towards the reference solution for increasing grid resolutions.

As a final note, the footprints of buildings and walls are superposed to all the figures referring to porous results for facilitating the comparison, even if they are not explicitly resolved in the computation.

#### *4.1 The Toce experimental case study*

Before proceeding with the application to real urban layouts and to the sensitivity analysis, the two methods are firstly compared considering the Toce River experiment (EU IMPACT project, Testa et al., 2007). The benchmark is a physical model in scale 1:100, which reproduces the flooding in the Toce valley (Northern Italy). A checkerboard building



layout with 18 square concrete building blocks of 15 cm side length is used to simulate the presence of an urban environment. Such a building arrangement has already been discussed in Sect. 3.3 and in Figure 5.

The porosity formulation recalled in Sect. 2.2 was already tested against this experimental benchmark using a uniform distribution of porosity parameters (Ferrari et al., 2019), but the successful application of the model required a particular value of conveyance porosity, obtained by collapsing two consecutive rows of buildings. Hence, it is not obvious that the algorithm for porosity computation is able to extract effective porosity distributions for the same schematic (but not trivial) building layout.

In the simulations, the initially dry domain is flooded by a 60 s long high inflow discharge entering the river (Testa et al., 2007), and a free outflow condition is specified at the end of the valley reach. The domain is characterized by a Manning roughness coefficient equal to  $n = 0.0162 \text{ m}^{-1/3}\text{s}$  (Testa et al., 2007). In the reference solution, buildings are explicitly resolved on a Cartesian grid with square cells of size  $\Delta x = 1 \text{ cm}$ ; the segment- and strip-based methods are used for the porous configuration with  $\Delta x = 5 \text{ cm}$ . Conveyance porosity is computed considering either a segment spacing  $d_{sg} = 5 \text{ mm}$  or a strip with  $d_{st} = L = 5 \text{ cm}$ .

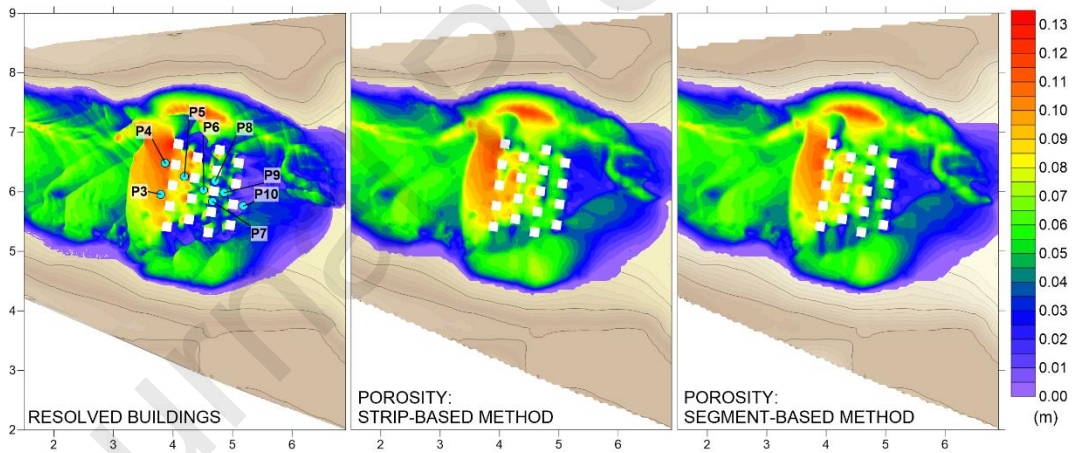


Figure 6. Toce River test. Water depths at  $t=14 \text{ s}$ . In background the bathymetry. The location of the gauge points is also reported.

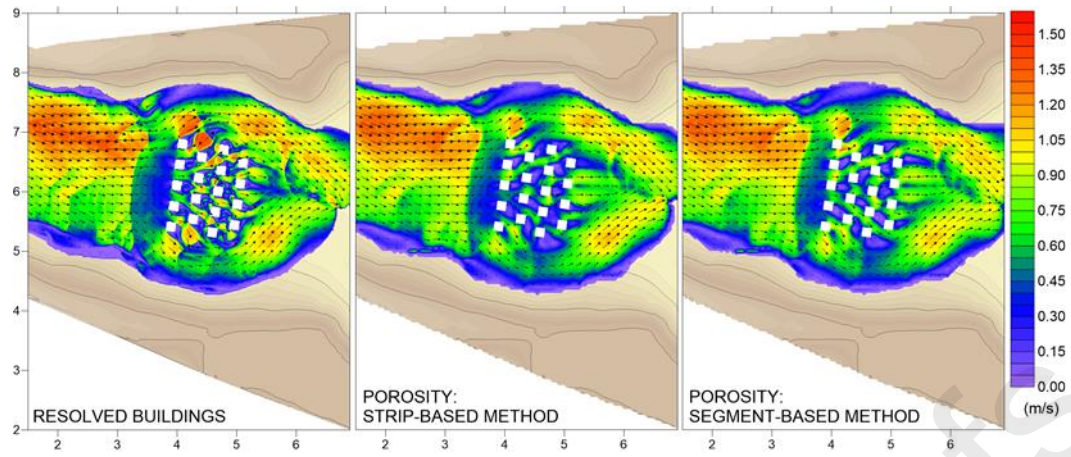


Figure 7. Toce River test. Water velocity at  $t=14$  s. In background the bathymetry.

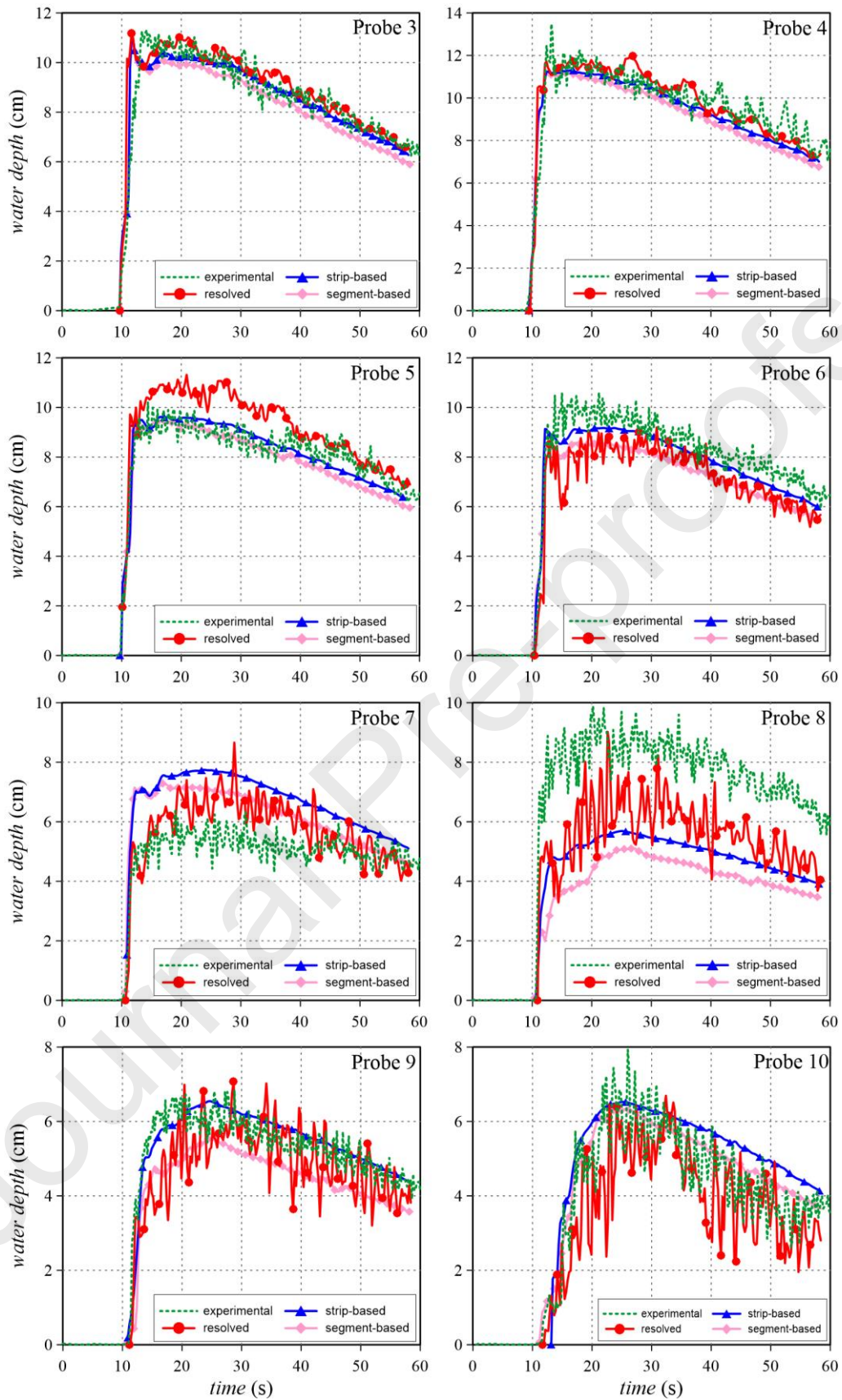


Figure 8. Toce River test. Water depths time series at gauge locations: comparison between the measured values and the results obtained with resolved buildings (red lines), the strip-based (blue lines) and the segment-based (pink lines) porosity parameters.

The water depths and velocities provided by the different methods are compared in Figure 6 (water depth) and Figure 7 (velocity) at time  $t = 14$  s. The comparison shows that both the segment- and strip-based methods allow reproducing the hydraulic jump that forms just upstream the obstacles and main flow features correctly. In particular, the velocity maps shown in Figure 7 highlight that the adoption of spatial distributed porosity fields allows describing the flow field variability within the urban area, and not only its effect on the external flow field (as in uniform porosity applications, Ferrari et al., 2019).

Figure 8 compares the water level time series recorded at gauge locations (Alcrudo et al., 2002; Testa et al., 2007) with those simulated by explicitly resolving the buildings and with the porosity parameters obtained with the strip- and segment-based methods. All the approaches provide similar results and show a generally good agreement with the measured values. Importantly, the use of spatially distributed porosity fields improves the model results, at the internal points P5 and P6, with respect to the uniform porosity parameters assumed in Ferrari et al. (2019).

The segment- and strip-based methods provide very similar results in this case; this is expected (see Sect. 3.3) considering that the resolution of the coarse grid (5 cm) is smaller than the geometrical length scale of the problem (buildings size is  $15 \times 15$  cm).

As discussed in Sect. 3.3, and in agreement with the schematic examples of Figure 4 and Figure 5, the strip-based method tends to provide lower values for  $\Psi_T$  than the segment-based method, resulting in slightly more dissipative scenarios; this is confirmed by the slightly larger water depths obtained with the strip-based method.

#### 4.2 *The Spinea district case study*

The first real urban layout here analyzed is a district in the town of Spinea, in Northern Italy (Figure 9). This middle-density area presents different-shaped buildings, which are separated one another by small walls, surrounded by gardens and courtyards, which act as temporally storage areas during flooding (Viero, 2019).

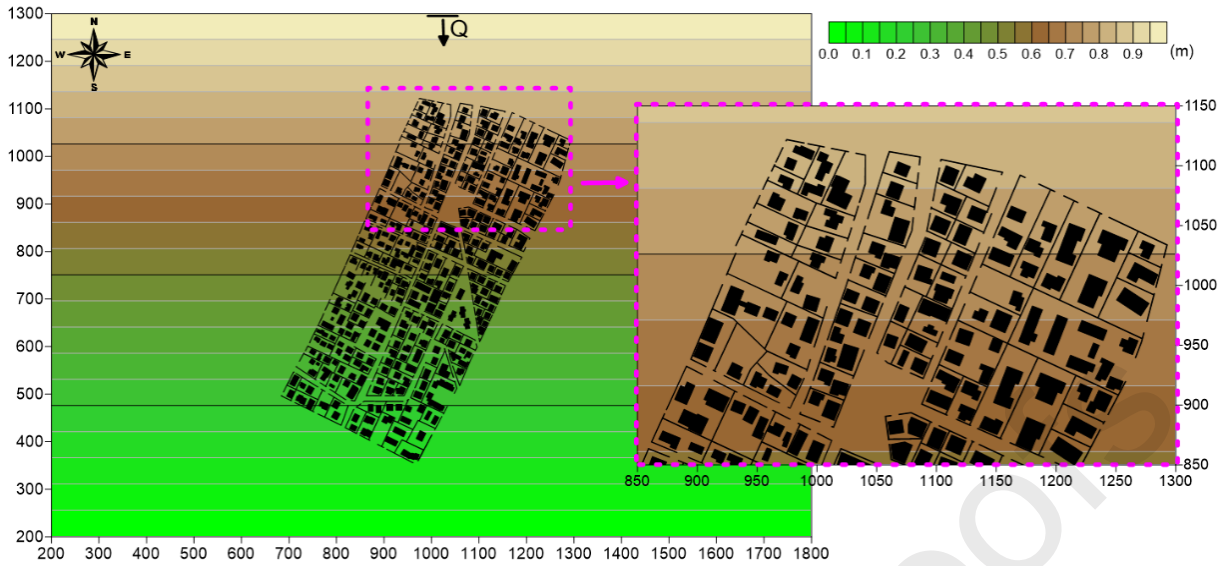


Figure 9. Spinea test. Bathymetry with the urban layout (dimensions in m).

In the simulations, the domain is characterized by a bottom slope of 0.09% (southward) and a Manning roughness coefficient  $n = 0.029 \text{ m}^{-1/3}\text{s}$ . The domain is initially dry; in the central 50 m of the northern edge, an inflow boundary condition is prescribed in the form of a 2-hours Gamma-distributed flood wave (Figure 10), with a peak value of about  $600 \text{ m}^3/\text{s}$ . Free outflow is assumed at the southern edge.

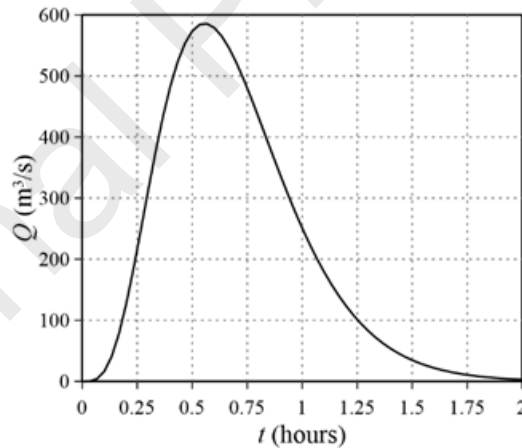


Figure 10. Spinea test. Inflow boundary condition.

The computational domain is discretized using a Cartesian grid with square cells of size  $\Delta x = 0.5 \text{ m}$  for the refined solution, and  $\Delta x = 2, 5, 10, 20$  and  $50 \text{ m}$  for the porous simulations. The porous tests adopt the porosity fields resulting from both the segment- and strip-based methods (for this latter case, different strip widths are considered). The main features of the simulations are reported in Table 1.

The model results, at the arrival of the flood peak ( $\approx 0.6 \text{ h}$ ), are shown in Figure 11 (water depths) and Figure 12 (velocity fields), for the reference simulation and for the porous applications with  $\Delta x = 5 \text{ m}$  and  $20 \text{ m}$ . Looking at the maps as a whole, it emerges

that the adoption of spatially distributed porosity parameters allows capturing the most relevant features of flooding both outside and inside the urbanized area. In terms of water depths (Figure 11), the porosity schemes capture the rise of the water depths north of the built-up area (orange-red zone) and the downstream drop (purple-blue zone south-east), with a slight loss of accuracy associated to grid coarsening (passing from ID:4 to ID:10 or, equivalently, from ID:5 to ID:13). In terms of velocity fields (Figure 12), the porosity schemes well capture the high velocity zone at the northern edge (orange-red), the middle one at west (green), and the low one at south-east (purple-blue). Differences with the reference solution can be found, essentially in terms of velocity, in external areas at the beginning or end of streets, due to the presence of singularities that only a resolved scheme on a fine mesh can capture properly.

The comparison of large-scale maps shows that the porosity fields provided by the segment- and by the strip-based methods, as for example test ID:4 or ID:10 (segments) against test ID:5 or ID:13 (strips), produce negligible differences in the simulated flow fields for grid resolutions of 5 and 20 m.

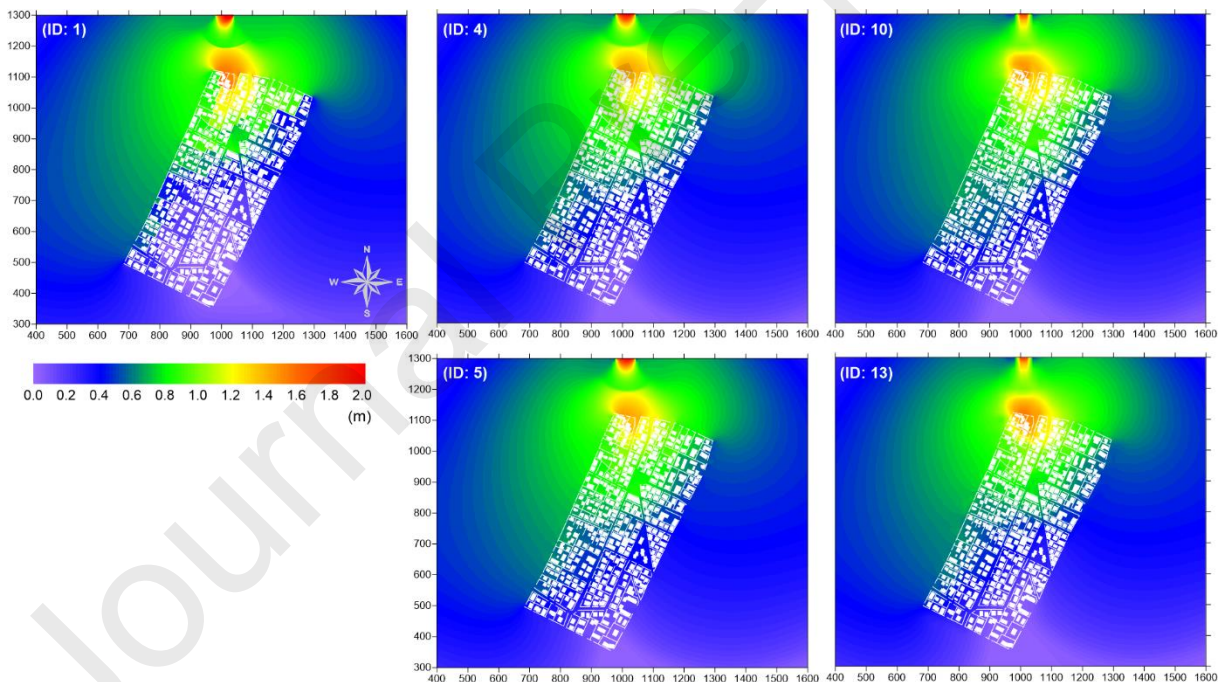


Figure 11. Spinea test. Water depth at the flood peak for the simulations with resolved buildings (ID:1), with porosity parameters evaluated using the segment-based method with  $\Delta x = 5$  m (ID:4) and  $\Delta x = 20$  m (ID:10), and the strip-based one with  $\Delta x = 5$  m (ID:5) and  $\Delta x = 20$  m (ID:13).

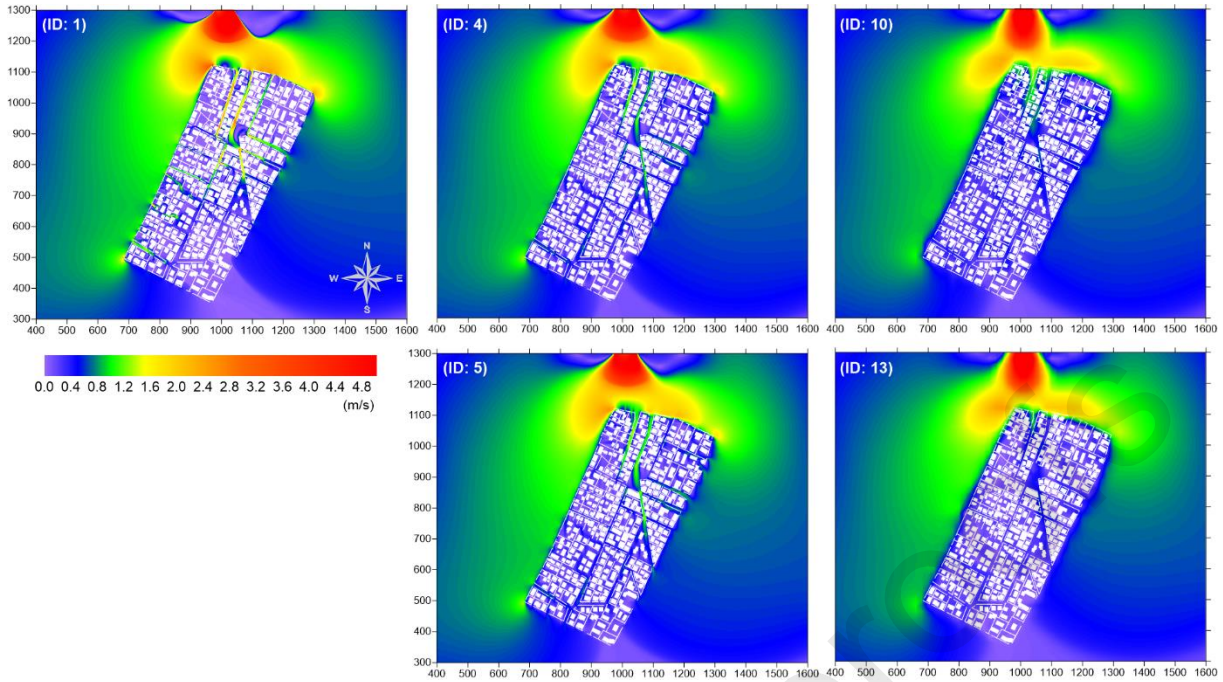


Figure 12. Spinea test. Velocity field at the flood peak for the simulations with resolved buildings (ID:1), with porosity parameters evaluated using the segment-based method with  $\Delta x = 5$  m (ID:4) and  $\Delta x = 20$  m (ID:10), and the strip-based one with  $\Delta x = 5$  m (ID:5) and  $\Delta x = 20$  m (ID:13).

Obviously, the results depend on the grid resolution: the simulations with  $\Delta x = 5$  m (ID:4, ID:5) agree with the reference solution (ID:1) better than the ones with  $\Delta x = 20$  m (ID:10, ID:13). The choice of a proper grid resolution is thus related to the flow field definition needed by the modeler, and not to specific requirements of the porosity approach.

Besides the large-scale analysis of the flow field around the built-up area, interesting information can be gained by looking at the inner velocity fields (Figure 13). As mentioned at the beginning of Sect. 3.1, the use of porosity models entails an unavoidable loss of details in the flow field within the urban area, essentially due to the adoption of coarse meshes in which buildings are not resolved explicitly. Nonetheless, the zoom view of Figure 13 shows that the use of spatially distributed porosity fields, evaluated with the methods of Sect. 3.2, allows reproducing the flow concentration along the main streets. Expectedly, the velocity values obtained in the reference solution (ID:1, with  $\Delta x = 0.5$  m) cannot be captured accurately with grids that are at least one order of magnitude coarser ( $\Delta x \geq 5$  m).

The comparison of ID:10 and ID:13 maps in Figure 13 shows that, for coarser grids, the strip-based method describes the blocking effects exerted by buildings and garden walls better than the segment-based method; indeed, in the western part of the built-up area, flow velocity is lower in ID:13 (purple colors) than in ID:10 (blue colors).

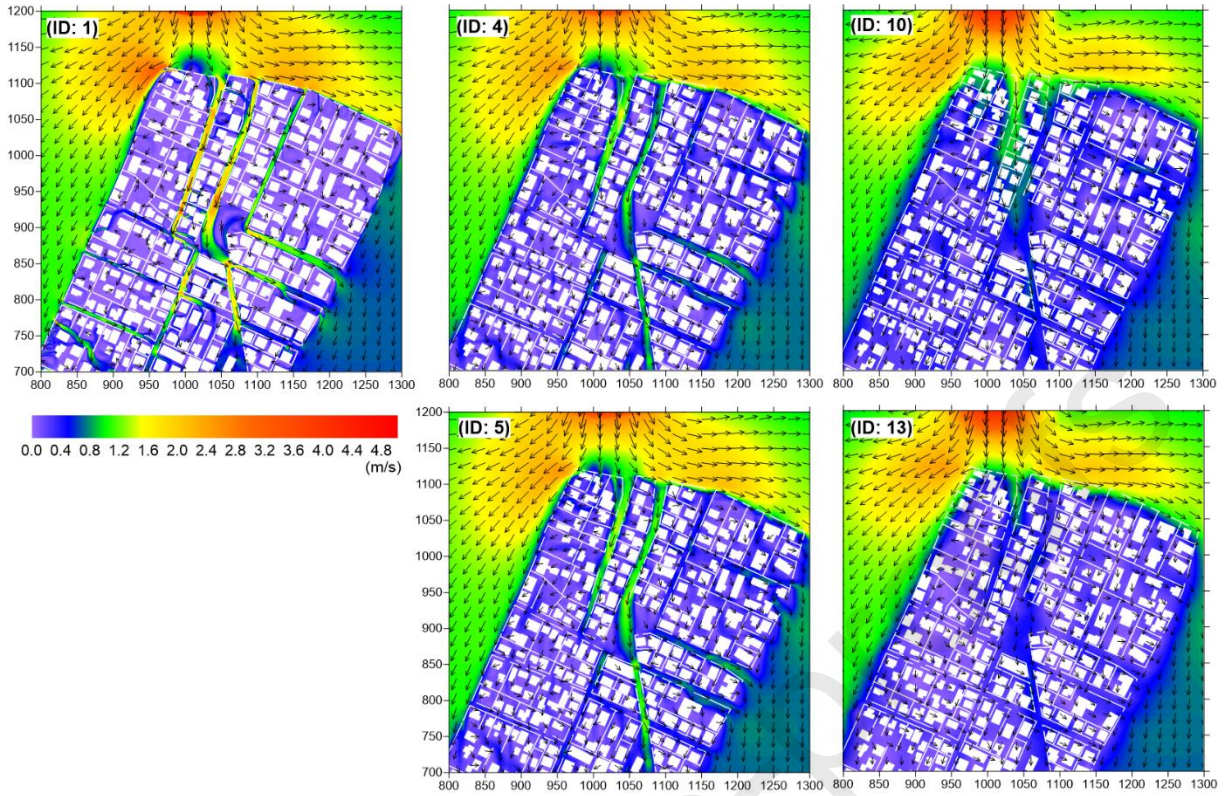


Figure 13. Spinea test. Zoom view of the velocity fields shown in Figure 12.

For the same time instant, Figure 14 compares the total depth indicator, which accounts for simultaneous water depth and velocity, representing the water depth at rest,  $D$ , whose static force is equivalent to the total force of the flow (Aureli et al., 2008; Ferrari et al., 2019) according to:

$$D = h\sqrt{1 + 2F} \quad (6)$$

where  $h$  represents the water depth and  $F$  the Froude number. The partition showed in the low-left panel of Figure 14 allows for the definition of the following classes: low ( $0 \leq D < 0.5$  m), medium ( $0.5 \leq D < 1$  m), high ( $1 \leq D < 1.5$  m) and very high ( $D \geq 1.5$  m).

Focusing on the effects exerted by the built-up area on the neighbouring ones, Figure 14 highlights that the porosity results well match with the reference one. Moreover, the porous scenarios capture the upper zone with high hazard level inside the urban patch, whereas they slightly overestimate the medium rank in the middle of the urban area.



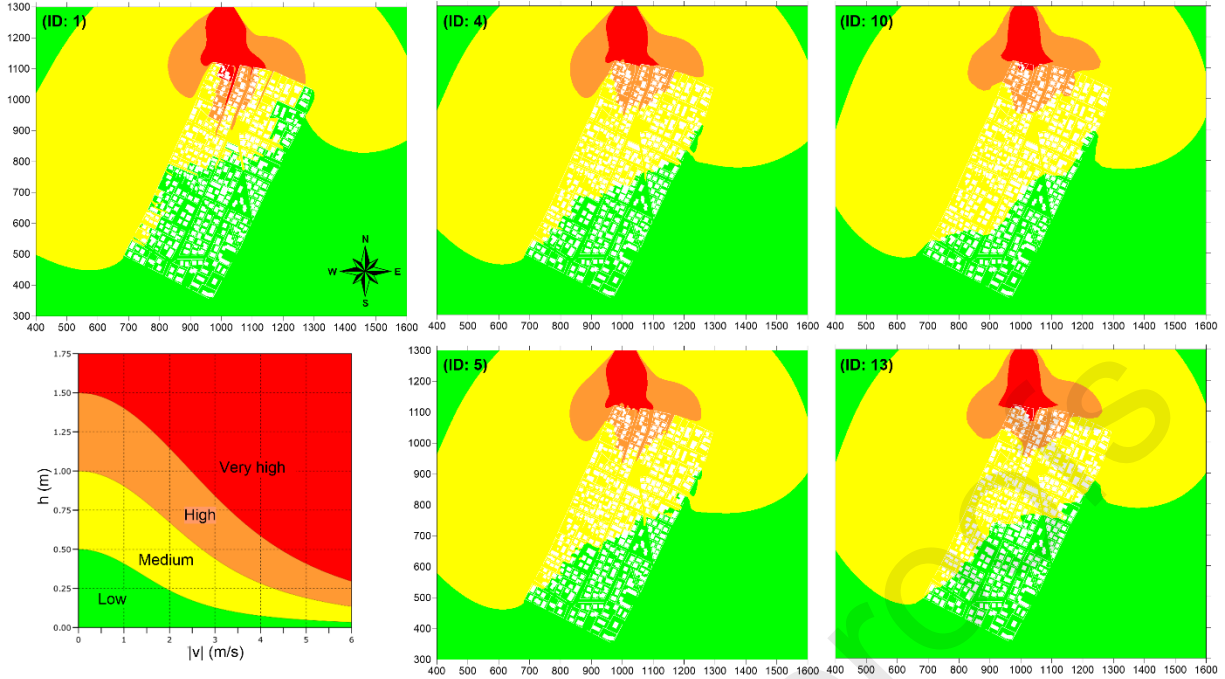


Figure 14. Spinea test. Total depth at the flood peak for the simulations with resolved buildings (ID:1), with porosity parameters evaluated using the segment-based method with  $\Delta x = 5$  m (ID:4) and  $\Delta x = 20$  m (ID:10), and the strip-based one with  $\Delta x = 5$  m (ID: 5) and  $\Delta x = 20$  m (ID:13). The  $h$ - $|v|$  plane relating the maximum total depth and the hazard degree is reported in the low left panel.

A more systematic analysis of the model performance, for all the simulations run, is carried out by quantifying the  $L_2$  error norm for the maximum water depth and the maximum velocity, according to:

$$L_2(f) = \sqrt{\frac{1}{N} \sum_{i=1}^N (f_{por}^i - f_{res}^i)^2} \quad (7)$$

where  $N$  denotes the number of computational cells,  $f$  is the variable of interest (maximum water depth,  $h_{max}$ , or velocity magnitude,  $u_{max}$ ), “por” and “res” subscripts identify the porous and reference solutions, respectively.

The analysis of error norms, reported in Table 1, gives further insights. The capability of both the segment- and strip-based methods in extracting reliable porosity parameters is confirmed by the relatively small values assumed by the error norms. Importantly, smaller error norms are obtained by increasing the grid resolution, indicating that the coarse solutions tend to the reference solution. The error norms increase significantly when passing from  $\Delta x \leq 20$  m to  $\Delta x = 50$  m, confirming the importance of choosing the grid size carefully on the base of the length-scale of the problem; in this case  $\Delta x = 50$  m denotes a cell size two order of magnitude larger than the reference one, and five times larger than the typical street width, which is about 10 m in this test (Figure 9). For a given grid resolution, the errors associated to the different methods (segments or strips) are similar to

each other for finer grids, whereas the strip-based method performs slightly better in the case of coarser grids (i.e., in line with the reasoning reported in Sect. 3.3).

Table 1. Spinea test. Simulation ID, modelling approach for the built-up area, method use for evaluating the porosity parameters, cell size  $\Delta x$ , cell number, run time  $t_{run}$ , norm of the maximum water depth  $L_2(h_{max})$  and of the maximum velocity  $L_2(u_{max})$ .

<i>ID</i>	Building modelling	Method	$\Delta x$ (m)	# cells ( $10^3$ )	$t_{run}$ (min)	$L_2(h_{max})$ (m)	$L_2(u_{max})$ ( $m \cdot s^{-1}$ )
1	Resolved	-	0.5	7045.4	119.47	-	-
2	Porosity	Segment	2	441.35	2.53	0.087	0.115
3	Porosity	Strip (2 m)	2	441.35	2.42	0.087	0.115
4	Porosity	Segment	5	70.94	0.24	0.087	0.127
5	Porosity	Strip (5 m)	5	70.94	0.25	0.090	0.126
6	Porosity	Segment	10	17.87	0.06	0.090	0.151
7	Porosity	Strip (1 m)	10	17.87	0.07	0.090	0.142
8	Porosity	Strip (2 m)	10	17.87	0.07	0.088	0.142
9	Porosity	Strip (10 m)	10	17.87	0.06	0.086	0.142
10	Porosity	Segment	20	4.54	0.03	0.096	0.179
11	Porosity	Strip (2 m)	20	4.54	0.03	0.095	0.180
12	Porosity	Strip (10 m)	20	4.54	0.03	0.095	0.174
13	Porosity	Strip (20 m)	20	4.54	0.03	0.092	0.174
14	Porosity	Segment	50	0.76	0.01	0.118	0.240
15	Porosity	Strip (10 m)	50	0.76	0.01	0.110	0.218
16	Porosity	Strip (50 m)	50	0.76	0.01	0.101	0.218

Finally, it is relevant to notice the high reduction of the runtimes that can be achieved in the porous simulations. As an example, the cases ID:2 and ID:3, which adopt the finest mesh here used for the porous simulations ( $\Delta x = 2$  m), run about 48 times faster than the simulation with resolved buildings (ID:1, 119.5/2.5). This gap enlarges up to two order of magnitude when using coarser meshes (e.g., 119.5/0.03).

### 4.3 The Palmanova town case study

The third model application deals with the modelling of a flood wave in a radial city as that of Palmanova (Northern Italy), in which buildings and streets converge to a central hexagon square (Figure 15). The goal is validating the effectiveness of the spatial distribution of porosity parameters, provided by the algorithms of Sect. 3.2, also in a real urban area characterized by a non-conventional building alignment.



Figure 15. Aerial view of the Palmanova town in Northern Italy, a particular example of radial city planning.

The domain, which is shown in Figure 16, is given a southward bottom slope of 0.08%. In the simulations, a Manning roughness coefficient  $n = 0.029 \text{ m}^{-1/3}\text{s}$  is assumed. As in the previous test, the initially dry domain is flooded by the 2 h long, Gamma-distributed flood wave shown in Figure 10; the upstream inflow boundary condition is prescribed in the central 50 m of the northern edge of the domain. Free outflow is assumed at the southern edge.

A Cartesian grid with square cells of size  $\Delta x = 0.4 \text{ m}$  is used to discretize the domain for the reference solution with resolved buildings, and  $\Delta x = 2, 5, 10$  and  $20 \text{ m}$  for the porous simulations. Again, the porous tests adopt the porosity fields resulting from both the segment- and strip-based methods and, for this latter case, different strip widths are considered. The main features of the simulations are reported in Table 2.

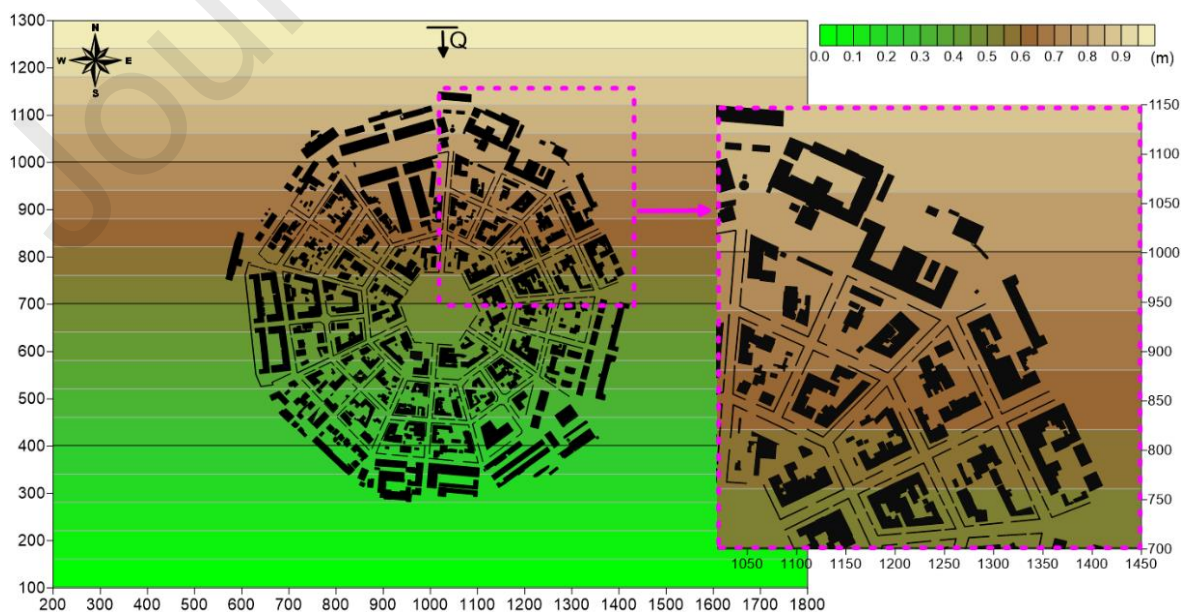


Figure 16. Palmanova test. Bathymetry with footprints of buildings and garden walls (dimensions in m).

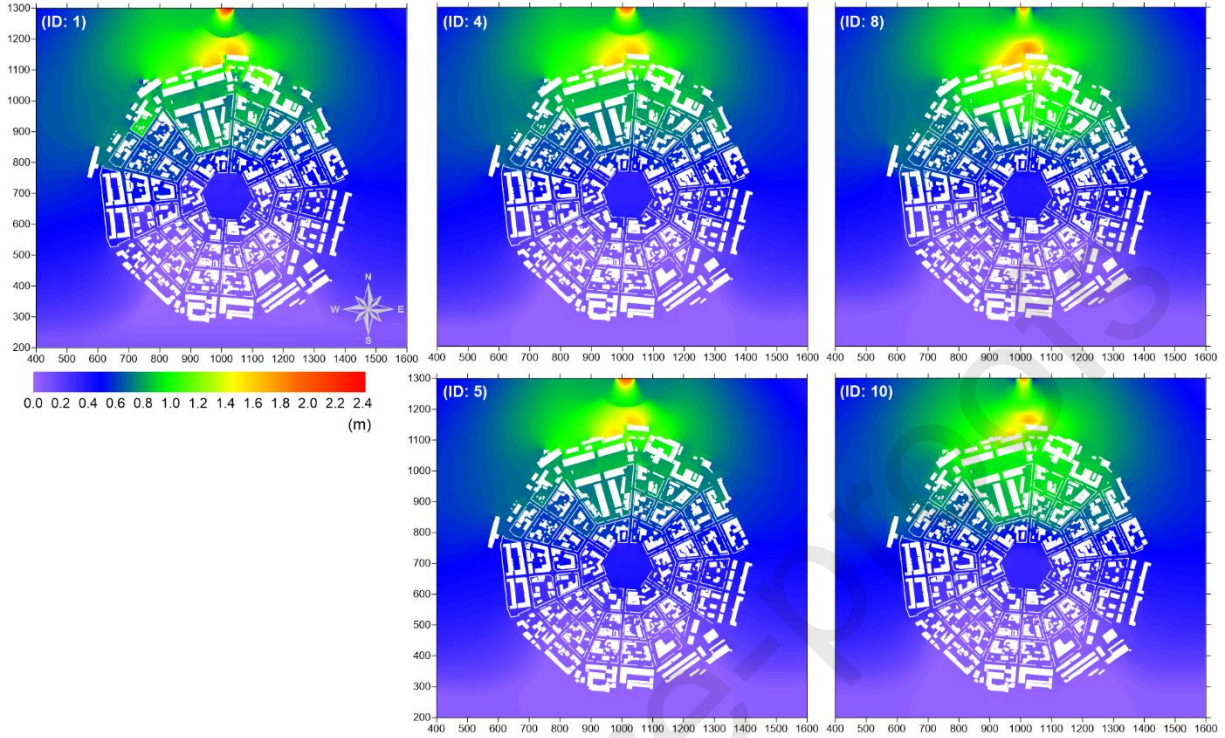


Figure 17. Palmanova test. Water depth at the flood peak for the simulations with resolved buildings (ID:1), with porosity parameters evaluated using the segment-based method with  $\Delta x = 5$  m (ID:4) and  $\Delta x = 20$  m (ID:8), and the strip-based one with  $\Delta x = 5$  m (ID:5) and  $\Delta x = 20$  m (ID:10).

Analogously to the previous test, the model results at the arrival of the flood peak ( $\approx 0.6$  h) are shown in Figure 17 (water depths) and Figure 18 (velocity fields), for the reference simulation and for the porous applications with  $\Delta x = 5$  m and 20 m. Compared with the reference solution (ID:1), the anisotropic porous solutions on the  $\Delta x = 5$  m grid (ID:4 and ID:5) well capture the deeper water depths at the entrance of the urban area (yellow-orange values), the flooding characteristics in the north part of the built-up zone (green values), and the low depth zone at south (purple values). Moreover, also for this urban layout, the segment- and strip-based methods show minimal differences with  $\Delta x = 5$  m and 20 m. For both the methods, the use of a coarser mesh size ( $\Delta x = 20$  m in ID:8 and ID:10) entails an excessive increment of the water depth inside the urban area (norther part) and, for this reason, it seems less adequate to model this scenario accurately.

A look at the velocity fields in Figure 18 confirms that the results with  $\Delta x = 5$  m (ID:4 and ID:5) match the reference solution (ID:1) well; the high flow velocity zone in the north part of the domain (orange-red values) and the medium one in the upstream semicircle (green zone) is captured quite accurately. The  $\Delta x = 20$  m grid confirms a loss of accuracy.

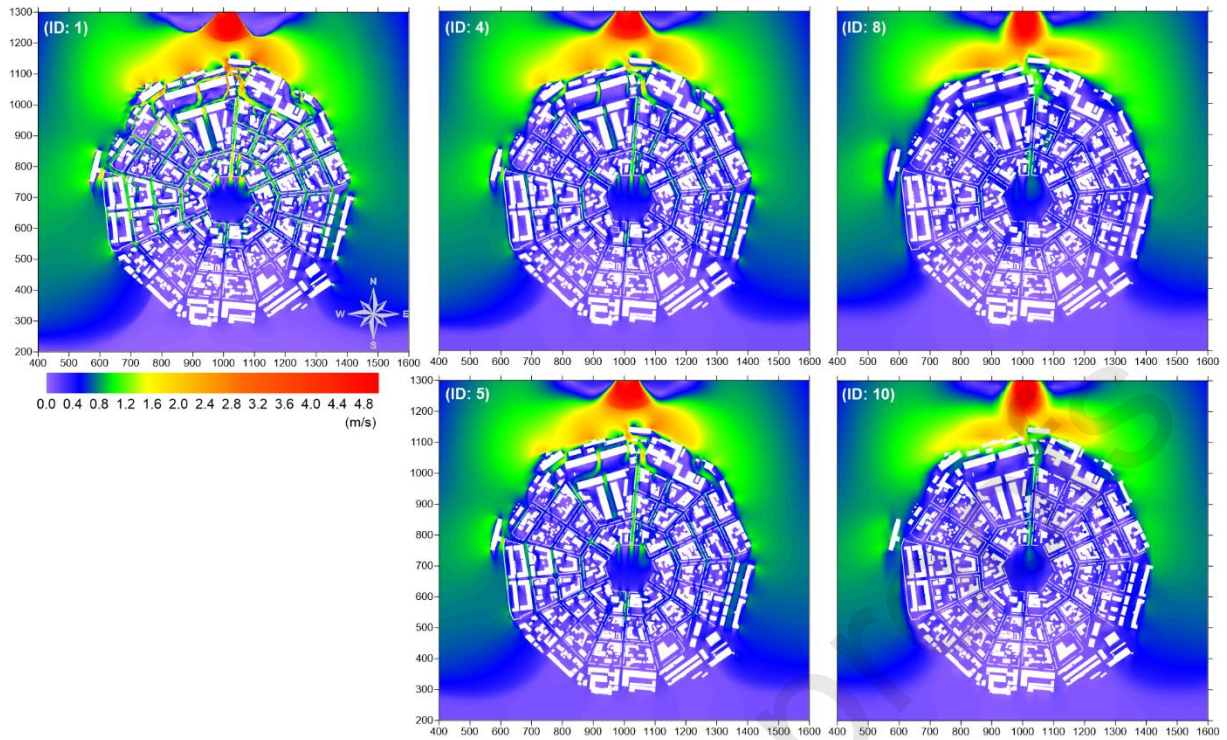


Figure 18. Palmanova test. Velocity field at the flood peak for the simulations with resolved buildings (ID:1), with porosity parameters evaluated using the segment-based method with  $\Delta x = 5$  m (ID:4) and  $\Delta x = 20$  m (ID:8), and the strip-based one with  $\Delta x = 5$  m (ID:5) and  $\Delta x = 20$  m (ID:10).

Importantly, the detailed view in Figure 19 reveals that the porous modelling allows for partially reproducing the flow field variability within the built-up area (ID: 4 and ID:5). Although only the high-resolution reference solution (ID:1) succeeds in modelling the flow field among small pathways, also the coarse grid allows identifying some preferential flow directions, with pathways characterized by larger flow velocities.

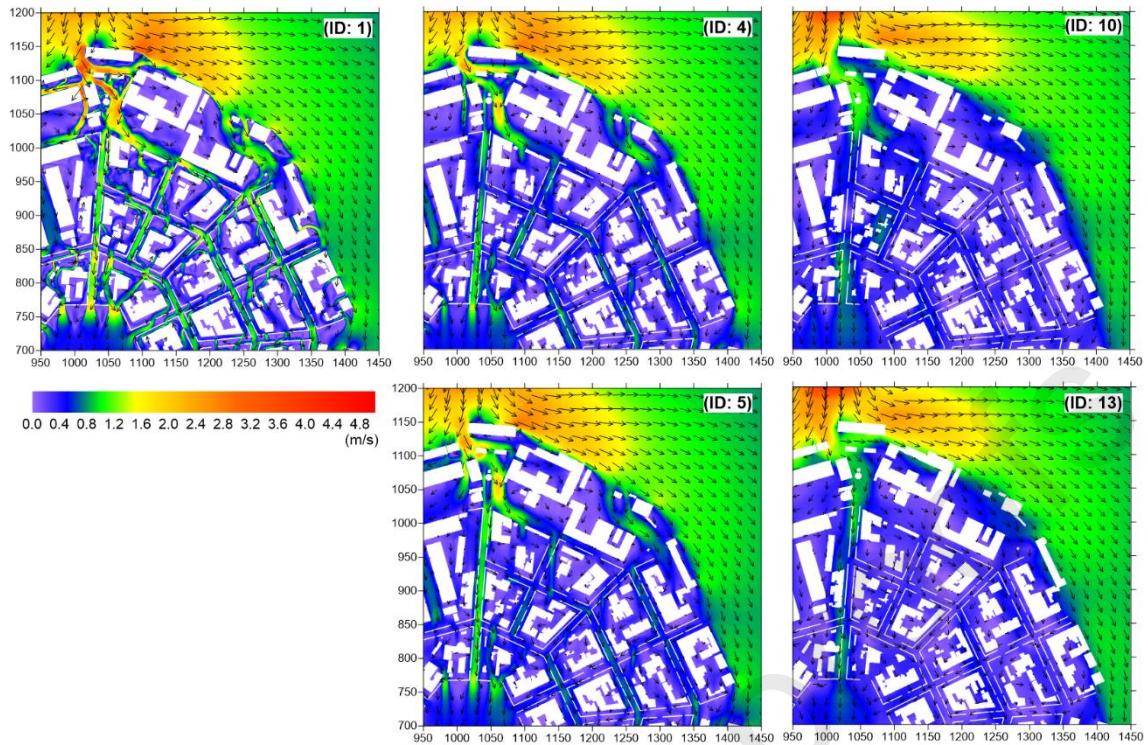


Figure 19. Palmanova test. Zoom view of the velocity fields shown in Figure 18.

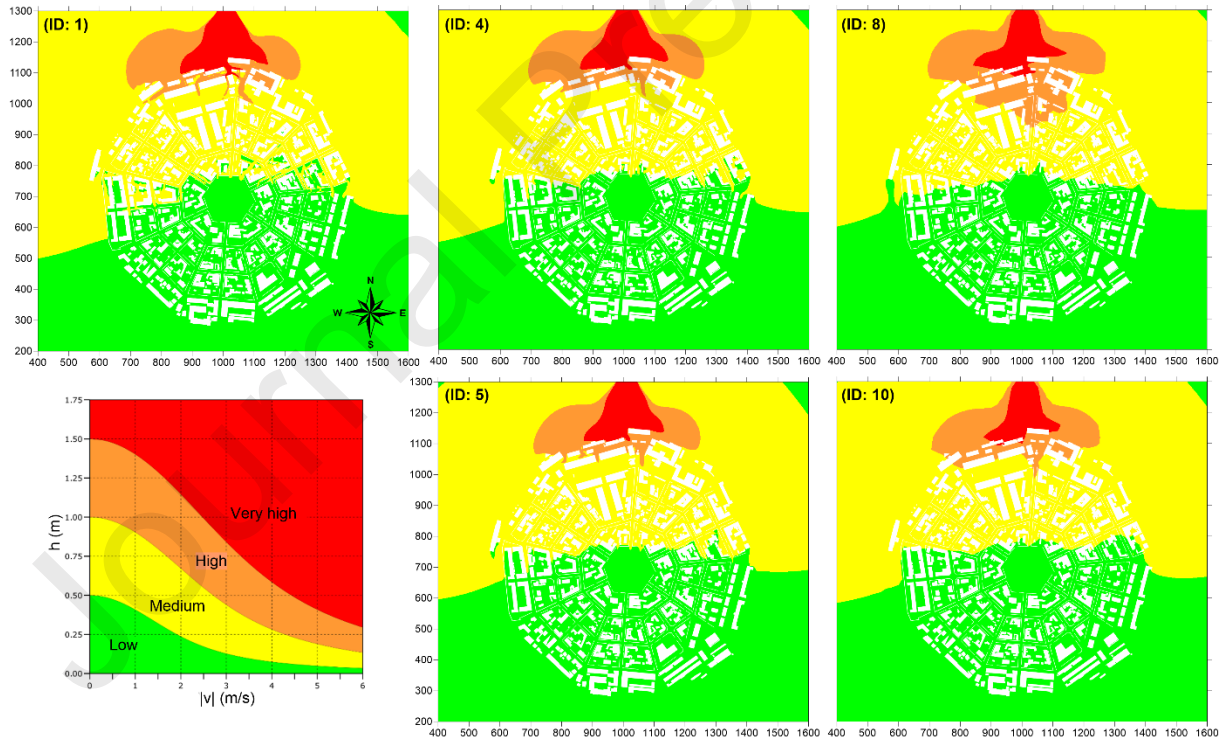


Figure 20. Palmanova test. Total depth at the flood peak for the simulations with resolved buildings (ID:1), with porosity parameters evaluated using the segment-based method with  $\Delta x = 5$  m (ID:4) and  $\Delta x = 20$  m (ID:8), and the strip-based one with  $\Delta x = 5$  m (ID:5) and  $\Delta x = 20$  m (ID:10). The  $h$ - $|v|$  plane relating the maximum total depth and the hazard degree is reported in the low left panel.

For the same time instant, Figure 20 compares the total depth indicator of Eq. (6) obtained from the different scenarios. The use of  $\Delta x = 5$  m grid resolution allows capturing the overall hazard rank regardless of the method used to extract the porosity fields, implying that such a grid size is suitable given the typical length scale of the problem. With the  $\Delta x = 20$  m grid, the segment-based method leads to an overestimation of the high hazard level in the north, whereas the strip-based method still provides accurate results, confirming that the strip-based method performs better on coarse grids.

With the aim of analyzing the model results quantitatively, the  $L_2$  error norms are evaluated according to Eq. (7) for both the maximum water depth and velocity magnitude (Table 2). The analysis leads to the same conclusions as in the Spinea test; model errors do not vary with the chosen algorithm (segment- or strip-based) significantly for lower mesh sizes, whereas the strip-based method is better suited for coarser grids. Moreover, when the mesh size is relatively large (e.g.,  $\Delta x = 20$  m), the errors increase significantly, essentially for the loss of details in describing the flow field within the built-up area.

Table 2. Palmanova test. Simulation ID, modelling approach for the built-up area, method for evaluating the porosity parameters, cell size  $\Delta x$ , cell number, run time  $t_{run}$ , norm of the maximum water depth  $L_2(h_{max})$  and of the maximum velocity  $L_2(u_{max})$ .

<i>ID</i>	Building modelling	Method	$\Delta x$ (m)	# cells ( $10^3$ )	$t_{run}$ (min)	$L_2(h_{max})$ (m)	$L_2(u_{max})$ ( $m \cdot s^{-1}$ )
1	Resolved	-	0.4	12007.0	250.56	-	-
2	Porosity	Segment	2	481.40	2.78	0.070	0.156
3	Porosity	Strip (2 m)	2	481.40	2.84	0.063	0.144
4	Porosity	Segment	5	77.36	0.26	0.077	0.202
5	Porosity	Strip (5 m)	5	77.36	0.26	0.066	0.176
6	Porosity	Segment	10	19.48	0.07	0.084	0.250
7	Porosity	Strip (10 m)	10	19.48	0.07	0.074	0.214
8	Porosity	Segment	20	4.94	0.03	0.104	0.283
9	Porosity	Strip (10 m)	20	4.94	0.03	0.088	0.267
10	Porosity	Strip (20 m)	20	4.94	0.03	0.086	0.271

Finally, the analysis of the runtimes reported in Table 2 further confirms the great advantage of the porous approach with respect to the explicit solution of buildings. For example, looking at cases ID:2 and ID:3 that still adopt a relatively fine grid ( $\Delta x = 2$  m), the computational burden is reduced up to 90 times if compared with the resolved simulation ( $250.56/2.78$ ).

## 5 Discussion and Conclusions

The present work dealt with a method to extract the spatial distribution of porosity parameters from building and obstacle footprints, to be used in the dual porosity model proposed by Viero (2019) and by Ferrari et al. (2019). A Fortran implementation of the algorithm is available, in a permanent repository, for free download and use (detailed information in Appendix A).

The key feature of the proposed method is the computation of the direction dependent conveyance porosity, which is performed by analysing the connectivity and the presence of preferential pathways within the cell, and not only at cell edges as in Integral Porosity models (Guinot et al., 2017; Sanders et al., 2008).

The effectiveness of the implemented method was assessed first by visual inspection, superposing the roseplots of conveyance porosity to the building footprints, to check the algorithm ability in detecting obstructions and preferential pathways correctly. Then, the porosity fields provided by the algorithm were used to simulate the flooding of experimental and real urban layouts with the porous version of the PARFLOOD model; the results were found to compare well with the reference solutions obtained using refined grids with explicitly resolved buildings.

The proposed method proved able to account for the presence of blocking features, which are known to affect the flow field substantially (Hodges, 2015; Li and Hodges, 2019), as well as for the role of large streets as preferential pathways and global flow pattern separators (Chen et al., 2018). The model application to experimental and real case studies suggests that the effects of restrictions are fairly reproduced, despite they are modelled through a modification of friction resistance only (Li and Hodges, 2020).

Notwithstanding the considerable variability of porosity fields with the grid resolution, the results in terms of flow field characteristics (water depths and velocities) were limited to the expected loss of accuracy associated with grid coarsening, confirming the substantial independence of the porosity approach to the computational grid.

It's worth stressing that the proposed method was conceived in the framework of large-scale, subgrid modelling of major flooding events in urbanized areas. Specific attention was paid to reproduce the effects exerted by the main obstacles that characterize complex urban layouts; urban micro-features, which can significantly influence the simulated inundation extent and depth (Mignot et al., 2013; Wang et al., 2018; Yu and Lane, 2011), were not considered for now.

As a final note, Viero (2019) warned that assuming the existence of two, reciprocally orthogonal, principal directions for the conveyance porosity is likely too simplistic to capture the complexity of real urban settlements under general conditions. The application of the methods presented above shows that the cell conveyance is well represented by the



tensor formulation with two reciprocally orthogonal principal directions, in particular when it is mainly determined by the presence of a single dominant obstacle. On the contrary, in the presence of multiple (either aligned or staggered) obstacles within a cell, the conveyance function  $\Psi(\alpha)$  presents multiple maxima and minima (for example, see the three local maxima in the green roseplot of Figure 5d), which reveal the presence of multiple preferential pathways along different directions. In such cases, the tensor formulation proposed by Viero (2019) and Ferrari et al. (2019) cannot reproduce the peculiar behaviours of  $\Psi(\alpha)$  properly. In assessing the case of aligned buildings, Velickovic et al. (2017) proposed to use drag terms along with suitable amplification coefficients depending on the flow direction, a solution then questioned by Guinot (2017b). Alternative formulations of the porosity model should be explored to this purpose.

**Acknowledgments.** R. Vacondio, P. Mignosa, and A. Defina are gratefully acknowledged for fruitful discussions. The editor, the associate editor, and the reviewers are also kindly acknowledged for their valuable suggestions on the early version of the manuscript. This research benefits from the HPC (High Performance Computing) facility of the University of Parma, Italy.

**Funding.** This research did not receive any specific grant from funding agencies in the public, commercial, or not-for-profit sectors.

## Appendix A. Algorithm for porosity computation

A Fortran implementation of the algorithm for computing the spatial distribution of the four porosity parameters is made available for free download and use in a permanent repository (<http://dx.doi.org/10.17632/47ypvbx9vm.1>). The repository also contains the input (and some output) files for the three case studies analyzed in the paper, as applicative examples.

The code reads geometric data of the polygon footprints in vector form from a .BLN file (Surfer ASCII), and the characteristics (cell size, location, and extent) of the numerical grid in the form of an .ASC (ESRI ASCII) file header. The output files are put in a specific subfolder, whose name includes the .ASC filename, the method used (segments or strips), and the value of segment spacing or strip width. As output files, the code can produce:

- four .xyz files (ASCII) with the coordinates of the cell center and the specific porosity parameter (one file per each parameter);
- four .ASC file (ESRI ASCII) with the spatial distribution of the specific porosity parameter (one file per each parameter, same information as in the above .xyz files);

- one .DXF file (AutoCAD ASCII) with building footprints, grid cells, conveyance roseplots, segments identifying the  $L$  and  $T$  principal directions;
- one .BLN file (Surfer ASCII) with building footprints, grid cells, conveyance roseplots, segments identifying the  $L$  and  $T$  principal directions;
- one .CNT file (ASCII, similar to the BLN format) with building footprints, grid cells, conveyance roseplots, segments identifying the  $L$  and  $T$  principal directions.

A configuration file in text format, to be placed in the same folder of the executable, allows choosing the output files to be produced; if the code cannot find this file, it will produce all the output files.

The code contains some optimizations that allow for a fast porosity computation. First, the polygons identifying the building footprints are ordered according to the  $x$  coordinate. Then, for each grid cell, the code identifies the (potentially) overlapping polygons, and processes only these ones in order to compute the storage and the conveyance porosity.

The algorithm performs the operations described in Sect. 3.2. Some additional details concerning the point n. 5 of the algorithm are given herein. With reference to the segment-based method (Sect. 3.2.1), the code performs the following operations:

- 5a) search all the intersection points between the sampling segment and the sides of the obstacle footprints. If no intersections are found, check if the whole segment is contained within any polygon (this occurs if the segment center falls within at least one polygon): if so, the free length is zero; otherwise, the algorithm continues as follows;
- 5b) order the intersection points based on the distance from the first endpoint of the sampling segment;
- 5c) check if each part of the sampling segment, between two consecutive intersection points, is contained within a polygon (i.e., the segment part overlaps a building footprint), to determined possible polygon overlapping;
- 5d) the free length of the segment is obtained by subtracting the length of all the overlapping parts, taking care of accounting for multiple overlapping only once (this may occur in the case of duplicated polygons).

Similarly, with reference to the strip-based method (Sect. 3.2.2), the code performs the following operations:

- 5a) search all the intersections between the strip edges and the sides of the obstacle footprints. If no intersections are found, check if the whole strip is contained within any polygon (this occurs if the strip center falls within at least one polygon): if so, the free length is zero; otherwise, the algorithm continues as follows;

- 5b) compute the projection of the intersections on the strip axis (starting and ending points for each projection). The projections are marked as “overlapping parts” of the strip axes;
- 5c) order the projections based on the distance from the first endpoint of the sampling segment to the starting point of the projection;
- 5d) check if each part of the strip axis, which is free of intersection projections, is contained within a polygon. If so, also these parts of strip axis are marked as “overlapping parts”;
- 5e) the free length of the strip axis is obtained by subtracting the length of all the “overlapping parts”, taking care of accounting for multiple overlapping only once (this may occur in the case of duplicated polygons or, more frequently, when different polygons intersect a single strip, and only the projections on the strip axis overlap).

## References

- Alcrudo, F., Garcia-Navarro, P., Brufau, P., Murillo, J., Garcia, D., Mulet, J., Testa, G., Zuccalà, D., 2002. The Model City Flooding Experiment, in: Proc. 2nd Project Workshop EC Contract EVG1-CT-2001-00037 IMPACT Investigation of Extreme Flood Processes and Uncertainty. Mo i Rana (Norway), p. 17.
- Arnell, N.W., Gosling, S.N., 2016. The impacts of climate change on river flood risk at the global scale. *Clim. Change* 134, 387–401. <https://doi.org/10.1007/s10584-014-1084-5>
- Arrault, A., Finaud-Guyot, P., Archambeau, P., Bruwier, M., Erpicum, S., Piroton, M., Dewals, B., 2016. Hydrodynamics of long-duration urban floods: experiments and numerical modelling. *Nat. Hazards Earth Syst. Sci.* 16, 1413–1429. <https://doi.org/10.5194/nhess-16-1413-2016>
- Aureli, F., Maranzoni, A., Mignosa, P., Ziveri, C., 2008. 2D numerical modelling for hydraulic hazard assessment: a dam-break case study, in: Altinakar, M., Kokpinar, M.A., Darama, Y., Yegen, B., Harmancioglu, N.B. (Eds.), *River Flow 2008, Proceedings of the International Conference on Fluvial Hydraulics*. Kubaba, Cesme, Izmir, Turkey, pp. 729–736.
- Braschi, G., Gallati, M., 1989. Simulation of a levee-breaking submersion of planes and urban areas, in: *HYDROCOMP '89, Proceedings of the International Conference on Computational Modelling and Experimental Methods in Hydraulics*. Elsevier Applied

Sci., N. Y., pp. 117–126.

- Bruwier, M., Archambeau, P., Erpicum, S., Piroton, M., Dewals, B., 2017. Shallow-water models with anisotropic porosity and merging for flood modelling on Cartesian grids. *J. Hydrol.* 554, 693–709. <https://doi.org/10.1016/j.jhydrol.2017.09.051>
- Cea, L., Vázquez-Cendón, M.E., 2010. Unstructured finite volume discretization of two-dimensional depth-averaged shallow water equations with porosity. *Int. J. Numer. Methods Fluids* 62, 903–930. <https://doi.org/10.1002/flid.2107>
- Chen, A.S., Evans, B., Djordjević, S., Savić, D.A., 2012a. Multi-layered coarse grid modelling in 2D urban flood simulations. *J. Hydrol.* 470–471, 1–11. <https://doi.org/10.1016/j.jhydrol.2012.06.022>
- Chen, A.S., Evans, B., Djordjević, S., Savić, D.A., 2012b. A coarse-grid approach to representing building blockage effects in 2D urban flood modelling. *J. Hydrol.* 426–427, 1–16. <https://doi.org/10.1016/j.jhydrol.2012.01.007>
- Chen, S., Garambois, P.-A., Finaud-Guyot, P., Dellinger, G., Mosé, R., Terfous, A., Ghenaim, A., 2018. Variance based sensitivity analysis of 1D and 2D hydraulic models: An experimental urban flood case. *Environ. Model. Softw.* 109, 167–181. <https://doi.org/10.1016/j.envsoft.2018.08.008>
- Costabile, P., Costanzo, C., De Lorenzo, G., Macchione, F., 2020. Is local flood hazard assessment in urban areas significantly influenced by the physical complexity of the hydrodynamic inundation model? *J. Hydrol.* 580, 124231. <https://doi.org/10.1016/j.jhydrol.2019.124231>
- Cozzolino, L., Pepe, V., Cimorelli, L., D’Aniello, A., Della Morte, R., Pianese, D., 2018. The solution of the dam-break problem in the Porous Shallow water Equations. *Adv. Water Resour.* 114, 83–101. <https://doi.org/10.1016/j.advwatres.2018.01.026>
- D’Alpaos, L., Defina, A., D’Alpaos, L., Defina, A., 2007. Mathematical modeling of tidal hydrodynamics in shallow lagoons: A review of open issues and applications to the Venice lagoon. *Comput. Geosci.* 33, 476–496. <https://doi.org/10.1016/j.cageo.2006.07.009>
- Defina, A., 2000. Two-dimensional shallow flow equations for partially dry areas. *Water Resour. Res.* 36, 3251. <https://doi.org/10.1029/2000WR900167>

- Defina, A., D'Alpaos, L., Matticchio, B., 1994. A new set of equations for very shallow water and partially dry areas suitable to 2D numerical models., in: Molinaro, P., Natale, L. (Eds.), *Modelling Flood Propagation Over Initially Dry Areas*. American Society of Civil Engineers, New York, pp. 72–81.
- Defina, A., Viero, D.P., 2010. Open channel flow through a linear contraction. *Phys. Fluids* 22, 036602. <https://doi.org/10.1063/1.3370334>
- Ferrari, A., Dazzi, S., Vacondio, R., Mignosa, P., 2020a. Enhancing the resilience to flooding induced by levee breaches in lowland areas: a methodology based on numerical modelling. *Nat. Hazards Earth Syst. Sci.* 20, 59–72. <https://doi.org/10.5194/nhess-20-59-2020>
- Ferrari, A., Vacondio, R., Dazzi, S., Mignosa, P., 2017. A 1D–2D Shallow Water Equations solver for discontinuous porosity field based on a Generalized Riemann Problem. *Adv. Water Resour.* 107, 233–249. <https://doi.org/10.1016/j.advwatres.2017.06.023>
- Ferrari, A., Vacondio, R., Mignosa, P., 2020b. A second-order numerical scheme for the porous shallow water equations based on a DOT ADER augmented Riemann solver. *Adv. Water Resour.* 140, 103587. <https://doi.org/10.1016/j.advwatres.2020.103587>
- Ferrari, A., Viero, D.P., Vacondio, R., Defina, A., Mignosa, P., 2019. Flood inundation modeling in urbanized areas: A mesh-independent porosity approach with anisotropic friction. *Adv. Water Resour.* 125, 98–113. <https://doi.org/10.1016/j.advwatres.2019.01.010>
- Guinot, V., 2017a. Consistency and bicharacteristic analysis of integral porosity shallow water models. Explaining model oversensitivity to mesh design. *Adv. Water Resour.* 107, 43–55. <https://doi.org/10.1016/j.advwatres.2017.06.008>
- Guinot, V., 2017b. A critical assessment of flux and source term closures in shallow water models with porosity for urban flood simulations. *Adv. Water Resour.* 109, 133–157. <https://doi.org/10.1016/j.advwatres.2017.09.002>
- Guinot, V., 2012. Multiple porosity shallow water models for macroscopic modelling of urban floods. *Adv. Water Resour.* 37, 40–72. <https://doi.org/10.1016/j.advwatres.2011.11.002>
- Guinot, V., Delenne, C., Rousseau, A., Boutron, O., 2018. Flux closures and source term models for shallow water models with depth-dependent integral porosity. *Adv. Water*

- Resour. 122, 1–26. <https://doi.org/10.1016/j.advwatres.2018.09.014>
- Guinot, V., Sanders, B.F., Schubert, J.E., 2017. Dual integral porosity shallow water model for urban flood modelling. *Adv. Water Resour.* 103, 16–31. <https://doi.org/10.1016/j.advwatres.2017.02.009>
- Guinot, V., Soares-Frazaõ, S., 2006. Flux and source term discretization in two-dimensional shallow water models with porosity on unstructured grids. *Int. J. Numer. Methods Fluids* 50, 309–345. <https://doi.org/10.1002/flid.1059>
- Hodges, B.R., 2015. Representing hydrodynamically important blocking features in coastal or riverine lidar topography. *Nat. Hazards Earth Syst. Sci.* 15, 1011–1023. <https://doi.org/10.5194/nhess-15-1011-2015>
- Jongman, B., 2018. Effective adaptation to rising flood risk. *Nat. Commun.* 9, 1986. <https://doi.org/10.1038/s41467-018-04396-1>
- Jongman, B., Ward, P.J., Aerts, J.C.J.H., 2012. Global exposure to river and coastal flooding: Long term trends and changes. *Glob. Environ. Chang.* 22, 823–835. <https://doi.org/10.1016/j.gloenvcha.2012.07.004>
- Kim, B., Sanders, B., Famiglietti, J.S., Guinot, V., 2015. Urban flood modeling with porous shallow-water equations: A case study of model errors in the presence of anisotropic porosity. *J. Hydrol.* 523, 680–692. <https://doi.org/10.1016/j.jhydrol.2015.01.059>
- Kundzewicz, Z.W., Hegger, D.L.T., Matczak, P., Driessen, P.P.J., 2018. Flood-risk reduction: Structural measures and diverse strategies. *Proc. Natl. Acad. Sci. U. S. A.* 115, 12321–12325. <https://doi.org/10.1073/pnas.1818227115>
- Kurganov, A., Petrova, G., 2007. A second-order well-balanced positivity preserving central-upwind scheme for the Saint-Venant system. *Commun. Math. Sci.* 5, 133–160. <https://doi.org/10.4310/CMS.2007.v5.n1.a6>
- Li, Z., Hodges, B.R., 2020. On modeling subgrid-scale macro-structures in narrow twisted channels. *Adv. Water Resour.* 135, 103465. <https://doi.org/10.1016/j.advwatres.2019.103465>
- Li, Z., Hodges, B.R., 2019. Modeling subgrid-scale topographic effects on shallow marsh hydrodynamics and salinity transport. *Adv. Water Resour.* 129, 1–15. <https://doi.org/10.1016/j.advwatres.2019.05.004>

- Liang, Q., Borthwick, A.G.L., 2009. Adaptive quadtree simulation of shallow flows with wet-dry fronts over complex topography. *Comput. Fluids* 38, 221–234. <https://doi.org/10.1016/j.compfluid.2008.02.008>
- Liang, Q., Marche, F., 2009. Numerical resolution of well-balanced shallow water equations with complex source terms. *Adv. Water Resour.* 32, 873–884. <https://doi.org/10.1016/j.advwatres.2009.02.010>
- McClymont, K., Morrison, D., Beevers, L., Carmen, E., 2020. Flood resilience: a systematic review. *J. Environ. Plan. Manag.* 63, 1151–1176. <https://doi.org/10.1080/09640568.2019.1641474>
- Mel, R., Viero, D.P., Carniello, L., D’Alpaos, L., 2020. Optimal floodgate operation for river flood management: The case study of Padova (Italy). *J. Hydrol. Reg. Stud.* accepted.
- Mignot, E., Zeng, C., Dominguez, G., Li, C.-W., Rivière, N., Bazin, P.-H., 2013. Impact of topographic obstacles on the discharge distribution in open-channel bifurcations. *J. Hydrol.* 494, 10–19. <https://doi.org/10.1016/j.jhydrol.2013.04.023>
- Muis, S., Güneralp, B., Jongman, B., Aerts, J.C.J.H., Ward, P.J., 2015. Flood risk and adaptation strategies under climate change and urban expansion: A probabilistic analysis using global data. *Sci. Total Environ.* 538, 445–457. <https://doi.org/10.1016/j.scitotenv.2015.08.068>
- Özgen, I., Liang, D., Hinkelmann, R., 2015. Shallow water equations with depth-dependent anisotropic porosity for subgrid-scale topography. *Appl. Math. Model.* 40(17–18), 7447–7473. <https://doi.org/10.1016/j.apm.2015.12.012>
- Özgen, I., Zhao, J., Liang, D., Hinkelmann, R., 2016. Urban flood modeling using shallow water equations with depth-dependent anisotropic porosity. *J. Hydrol.* 541, 1165–1184. <https://doi.org/10.1016/j.jhydrol.2016.08.025>
- Radhakrishnan, M., Pathirana, A., Ashley, R.M., Gersonius, B., Zevenbergen, C., 2018. Flexible adaptation planning for water sensitive cities. *Cities* 78, 87–95. <https://doi.org/10.1016/j.cities.2018.01.022>
- Rong, Y., Zhang, T., Zheng, Y., Hu, C., Peng, L., Feng, P., 2020. Three-dimensional urban flood inundation simulation based on digital aerial photogrammetry. *J. Hydrol.* 584, 124308. <https://doi.org/10.1016/j.jhydrol.2019.124308>

- Sanders, B.F., 2017. Hydrodynamic Modeling of Urban Flood Flows and Disaster Risk Reduction. Oxford Res. Encycl. Nat. Hazard Sci. <https://doi.org/10.1093/acrefore/9780199389407.013.127>
- Sanders, B.F., Schubert, J.E., 2019. PRIMo: Parallel raster inundation model. *Adv. Water Resour.* 126, 79–95. <https://doi.org/10.1016/j.advwatres.2019.02.007>
- Sanders, B.F., Schubert, J.E., Gallegos, H.A., 2008. Integral formulation of shallow-water equations with anisotropic porosity for urban flood modeling. *J. Hydrol.* 362, 19–38. <https://doi.org/10.1016/j.jhydrol.2008.08.009>
- Schubert, J.E., Sanders, B.F., 2012. Building treatments for urban flood inundation models and implications for predictive skill and modeling efficiency. *Adv. Water Resour.* 41, 49–64. <https://doi.org/10.1016/j.advwatres.2012.02.012>
- Soares-Frazão, S., Franzini, F., Linkens, J., Snaps, J.-C., 2018. Investigation of distributed-porosity fields for urban flood modelling using single-porosity models. *E3S Web Conf.* 40, 06040. <https://doi.org/10.1051/e3sconf/20184006040>
- Soares-Frazao, S., Lhomme, J., Guinot, V., Zech, Y., 2008. Two-dimensional shallow-water model with porosity for urban flood modelling. *J. Hydraul. Res.* 46, 45–64. <https://doi.org/10.1080/00221686.2008.9521842>
- Tanoue, M., Hirabayashi, Y., Ikeuchi, H., 2016. Global-scale river flood vulnerability in the last 50 years. *Sci. Rep.* 6, 36021. <https://doi.org/10.1038/srep36021>
- Testa, G., Zuccalà, D., Alcrudo, F., Mulet, J., Soares-Frazão, S., 2007. Flash flood flow experiment in a simplified urban district. *J. Hydraul. Res.* 45, 37–44. <https://doi.org/10.1080/00221686.2007.9521831>
- Toro, E.F., 2001. *Shock-capturing methods for free-surface shallow flows*. John Wiley.
- Toro, E.F., 1999. *Riemann Solvers and Numerical Methods for Fluid Dynamics*. Springer.
- Vacondio, R., Aureli, F., Ferrari, A., Mignosa, P., Dal Palù, A., 2016. Simulation of the January 2014 flood on the Secchia River using a fast and high-resolution 2D parallel shallow-water numerical scheme. *Nat. Hazards* 80, 103–125. <https://doi.org/10.1007/s11069-015-1959-4>
- Vacondio, R., Dal Palù, A., Ferrari, A., Mignosa, P., Aureli, F., Dazzi, S., 2017. A non-



- uniform efficient grid type for GPU-parallel Shallow Water Equations models. *Environ. Model. Softw.* 88, 119–137. <https://doi.org/10.1016/j.envsoft.2016.11.012>
- Vacondio, R., Dal Palù, A., Mignosa, P., 2014. GPU-enhanced Finite Volume Shallow Water solver for fast flood simulations. *Environ. Model. Softw.* 57, 60–75. <https://doi.org/10.1016/j.envsoft.2014.02.003>
- Varra, G., Pepe, V., Cimorelli, L., Della Morte, R., Cozzolino, L., 2020. On integral and differential porosity models for urban flooding simulation. *Adv. Water Resour.* 136, 103455. <https://doi.org/10.1016/j.advwatres.2019.103455>
- Velickovic, M., Zech, Y., Soares-Frazaõ, S., 2017. Steady-flow experiments in urban areas and anisotropic porosity model. *J. Hydraul. Res.* 55, 85–100. <https://doi.org/10.1080/00221686.2016.1238013>
- Viero, D.P., 2019. Modelling urban floods using a finite element staggered scheme with an anisotropic dual porosity model. *J. Hydrol.* 568, 247–259. <https://doi.org/10.1016/j.jhydrol.2018.10.055>
- Viero, D.P., Peruzzo, P., Carniello, L., Defina, A., 2014. Integrated mathematical modeling of hydrological and hydrodynamic response to rainfall events in rural lowland catchments. *Water Resour. Res.* 50, 5941–5957. <https://doi.org/10.1002/2013WR014293>
- Viero, D.P., Roder, G., Matticchio, B., Defina, A., Tarolli, P., 2019. Floods, landscape modifications and population dynamics in anthropogenic coastal lowlands: The Polesine (northern Italy) case study. *Sci. Total Environ.* 651, 1435–1450. <https://doi.org/10.1016/j.scitotenv.2018.09.121>
- Viero, D.P., Valipour, M., 2017. Modeling anisotropy in free-surface overland and shallow inundation flows. *Adv. Water Resour.* 104, 1–14. <https://doi.org/10.1016/j.advwatres.2017.03.007>
- Viero, D. Pietro, D’Alpaos, A., Carniello, L., Defina, A., 2013. Mathematical modeling of flooding due to river bank failure. *Adv. Water Resour.* 59, 82–94. <https://doi.org/10.1016/j.advwatres.2013.05.011>
- Wang, Y., Chen, A.S., Fu, G., Djordjević, S., Zhang, C., Savić, D.A., 2018. An integrated framework for high-resolution urban flood modelling considering multiple information sources and urban features. *Environ. Model. Softw.* 107, 85–95.

<https://doi.org/10.1016/j.envsoft.2018.06.010>

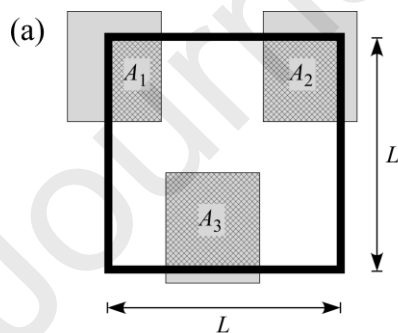
Wing, O.E.J., Bates, P.D., Smith, A.M., Sampson, C.C., Johnson, K.A., Fargione, J., Morefield, P., 2018. Estimates of present and future flood risk in the conterminous United States. *Environ. Res. Lett.* 13, 034023. <https://doi.org/10.1088/1748-9326/aaac65>

Yu, D., Lane, S.N., 2011. Interactions between subgrid-scale resolution, feature representation and grid-scale resolution in flood inundation modelling. *Hydrol. Process.* 25, 36–53. <https://doi.org/10.1002/hyp.7813>

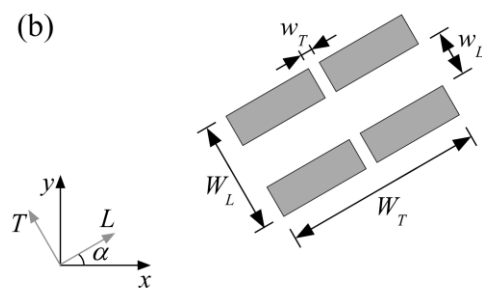
Yu, D., Lane, S.N., 2006. Urban fluvial flood modelling using a two-dimensional diffusion-wave treatment. Part 2: development of a sub-grid-scale treatment. *Hydrol. Process.* 20, 1567–1583. <https://doi.org/10.1002/hyp.5936>

**Highlights: (3 to 5 bullet points, max 85 characters including spaces)**

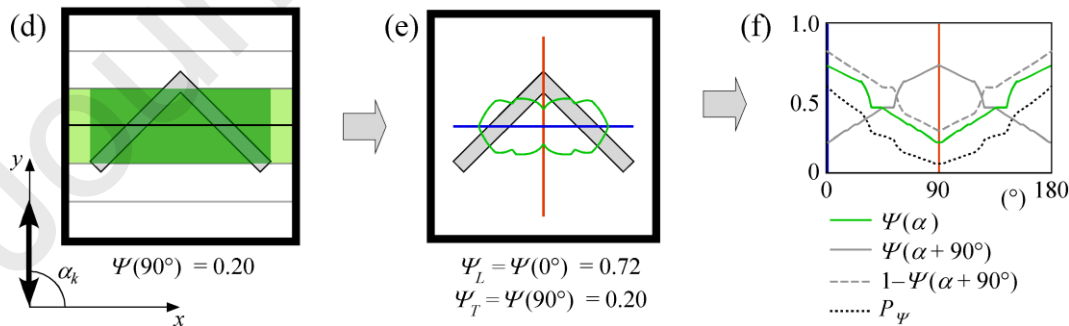
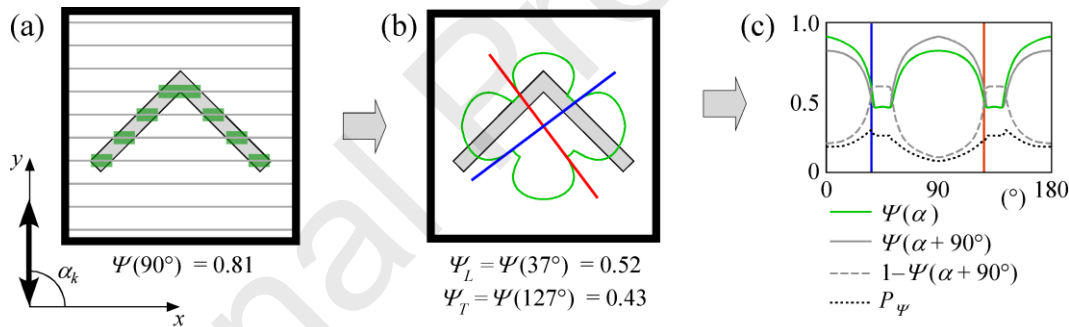
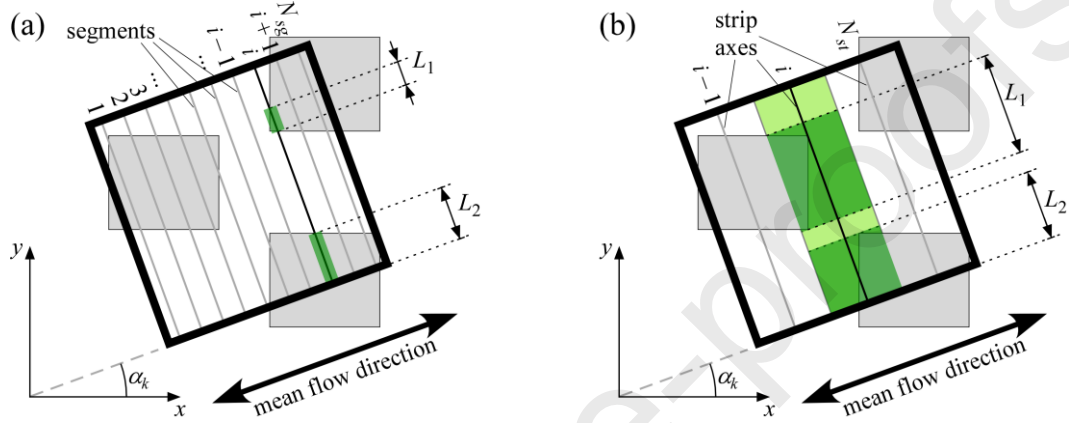
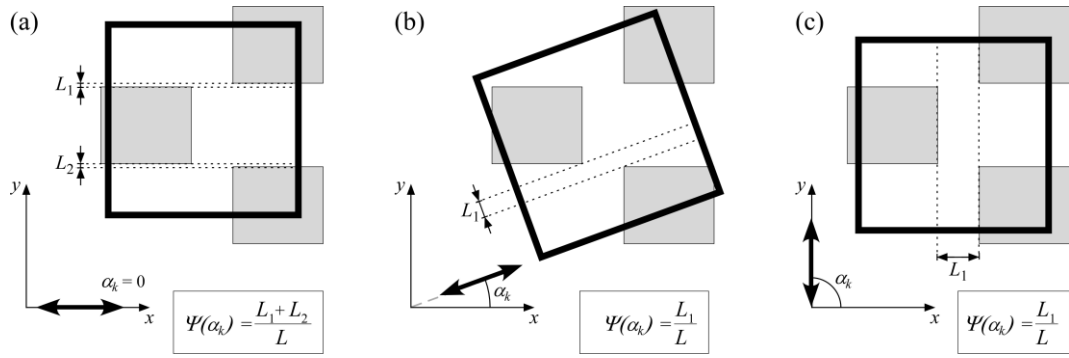
- Flood modelling in real urban areas is a challenge for differential anisotropic porosity models
- Directionally-dependent, cell-based conveyance porosity is not trivial to estimate
- A method is proposed to extract conveyance porosity fields from building footprints
- Straightforward application to complex, real urban layouts provides accurate results
- A Fortran numerical implementation of the proposed method is made available

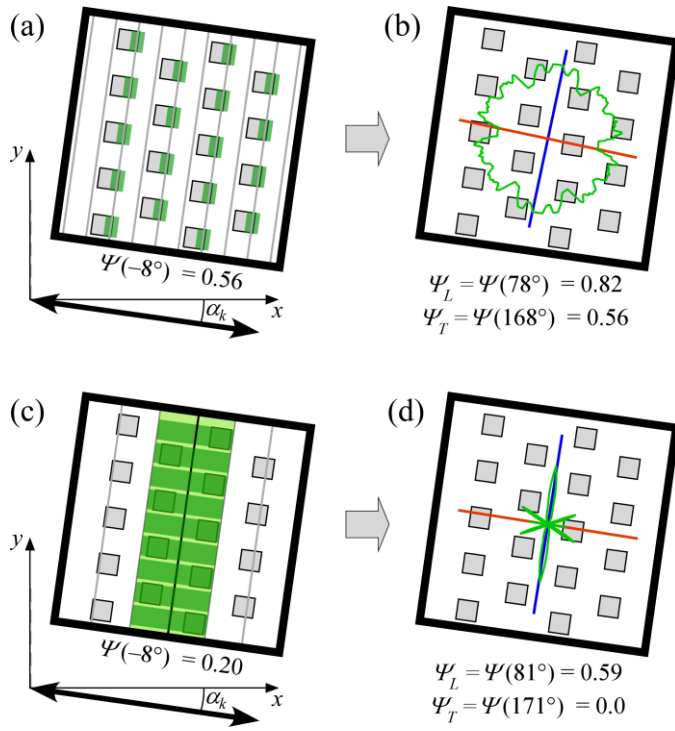


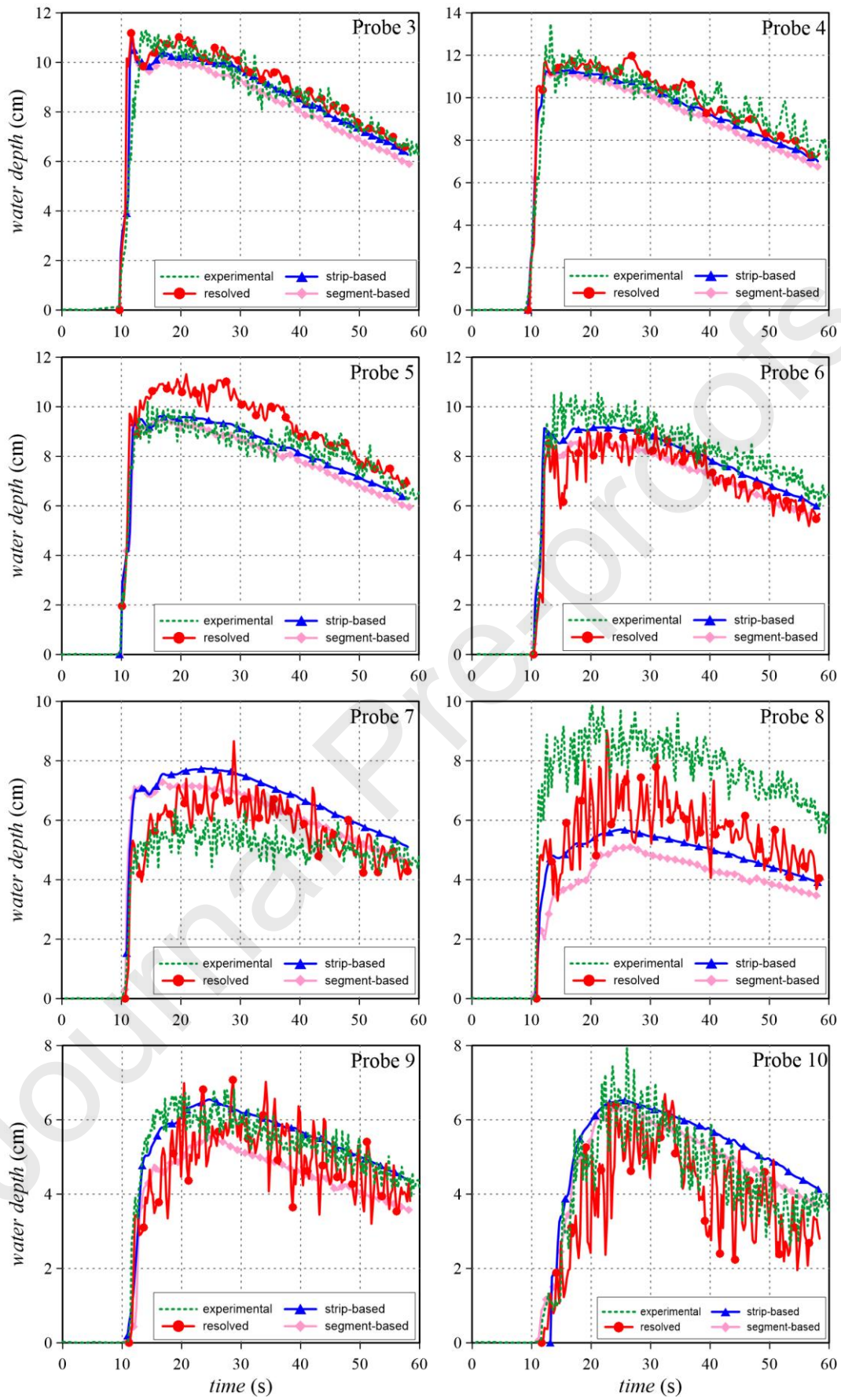
$$\phi = 1 - \frac{A_1 + A_2 + A_3}{A_{cell}}$$

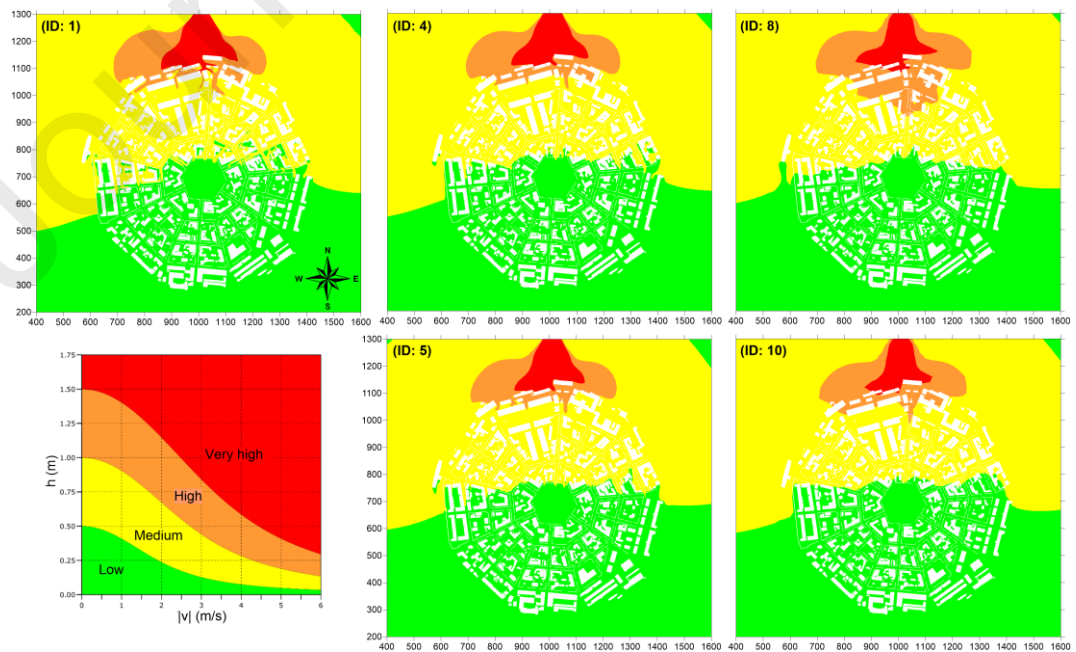
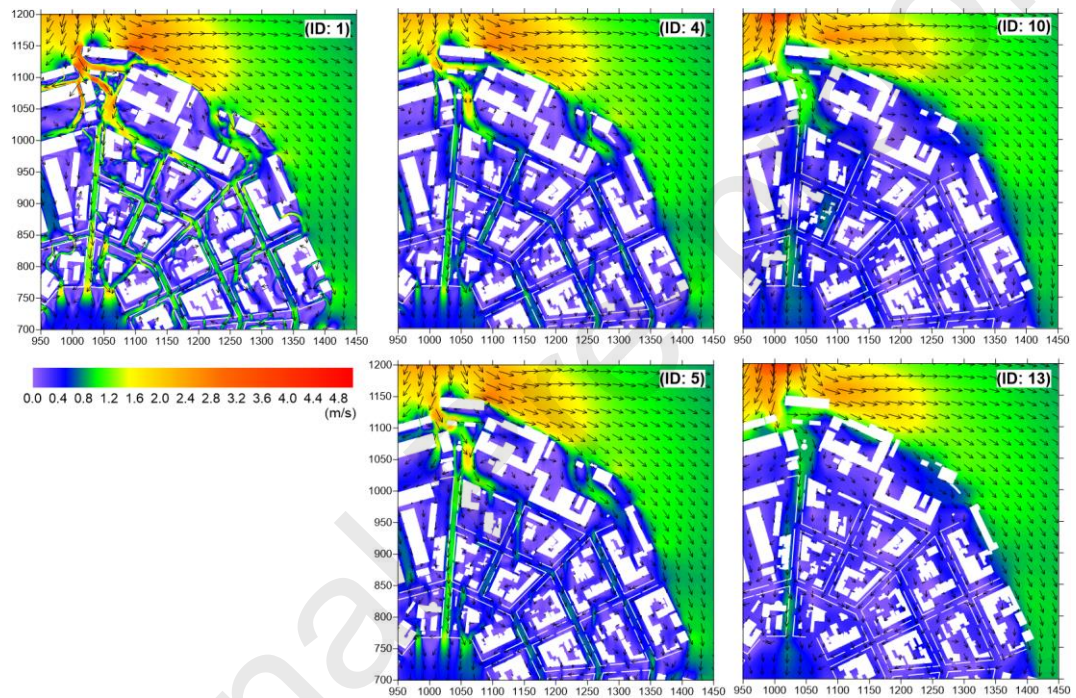
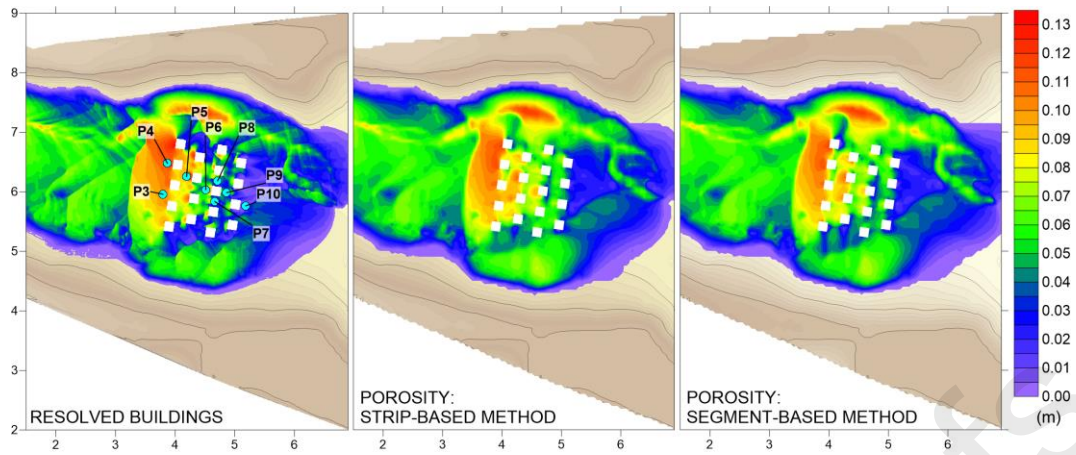


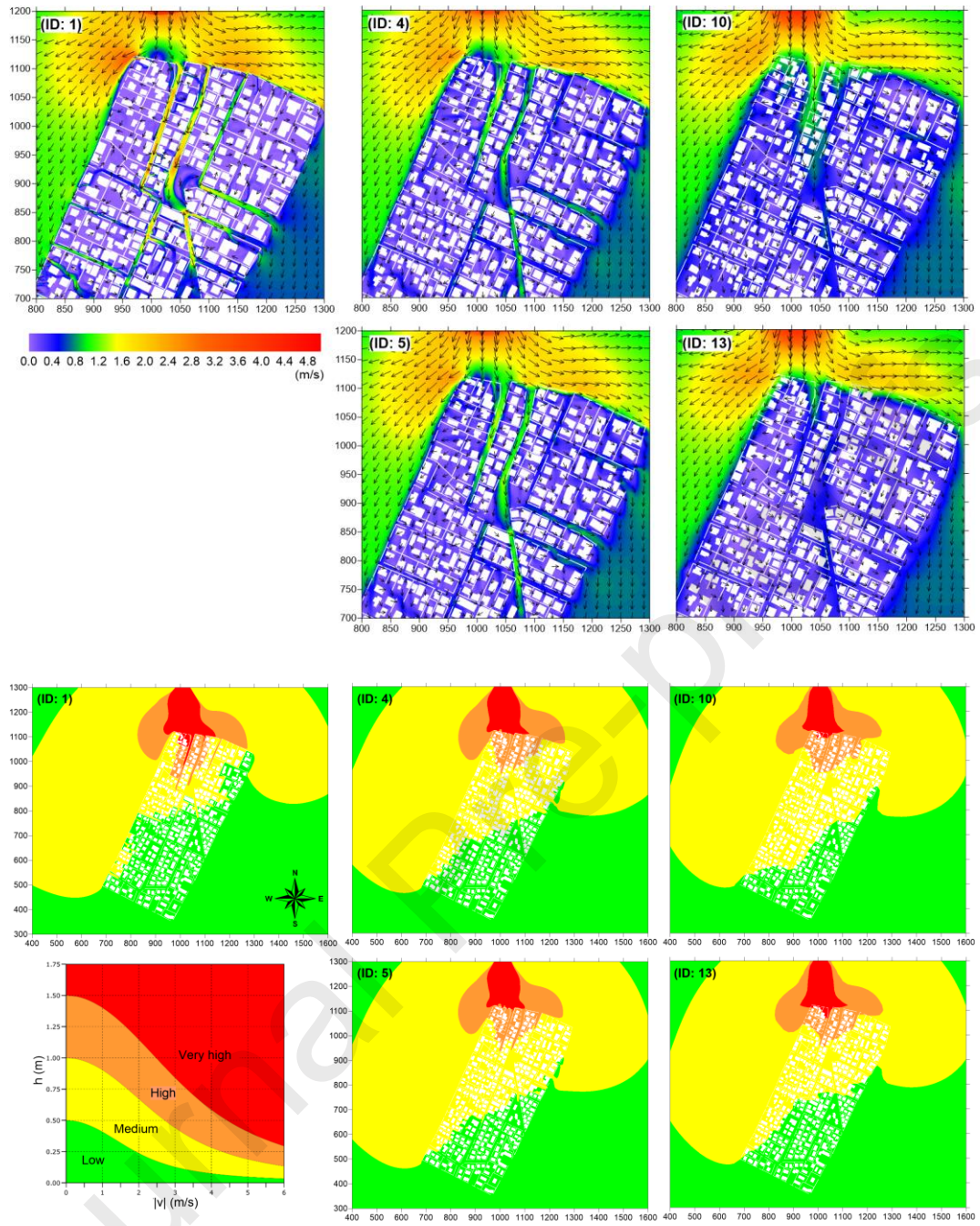
$$\Psi_L = \frac{w_L}{W_L} \quad \Psi_T = \frac{w_T}{W_T}$$

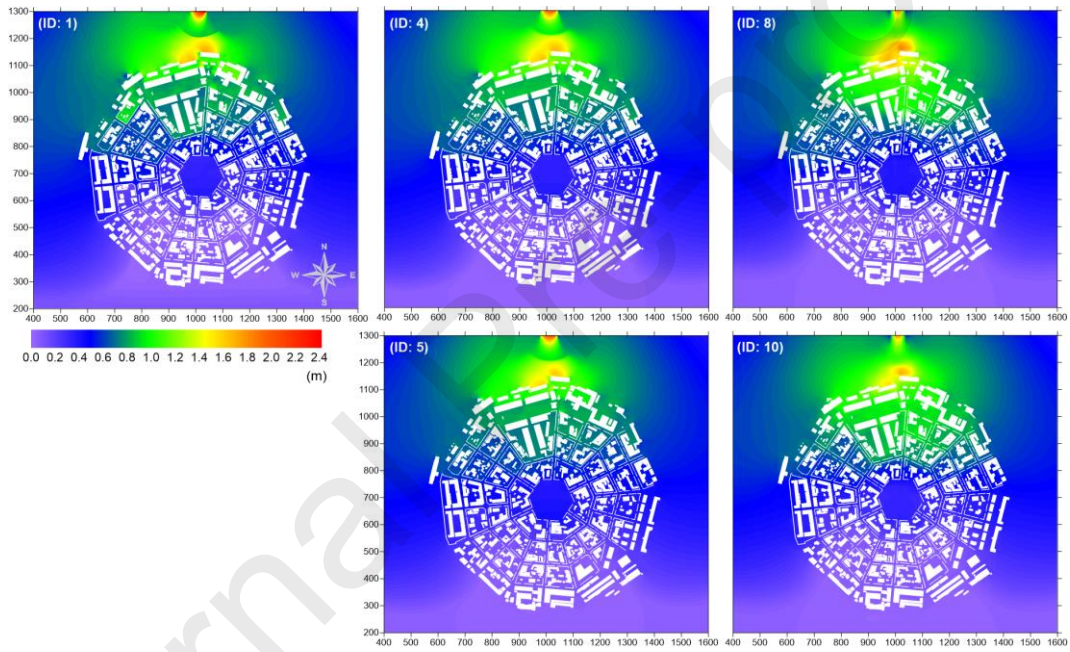
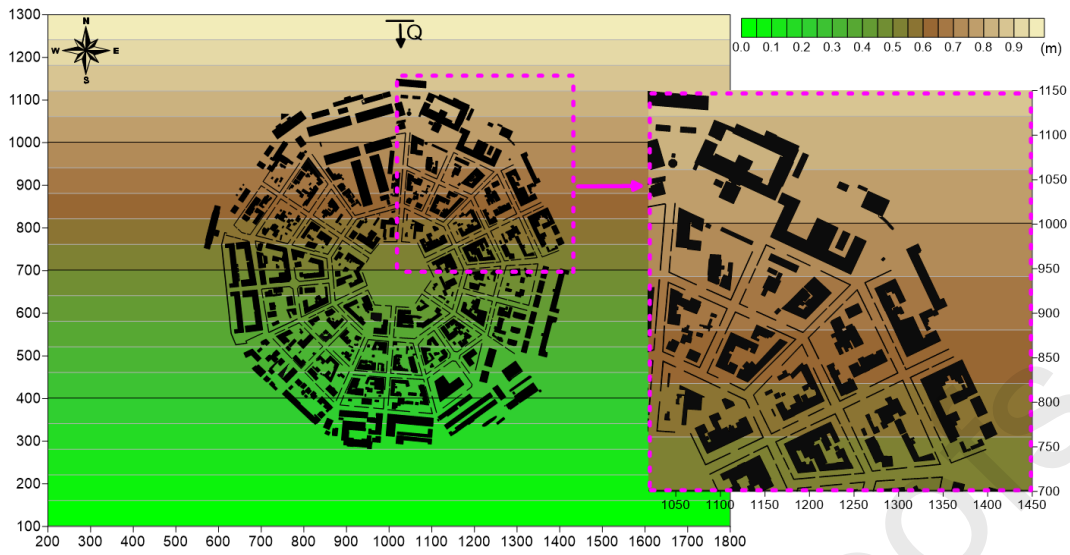




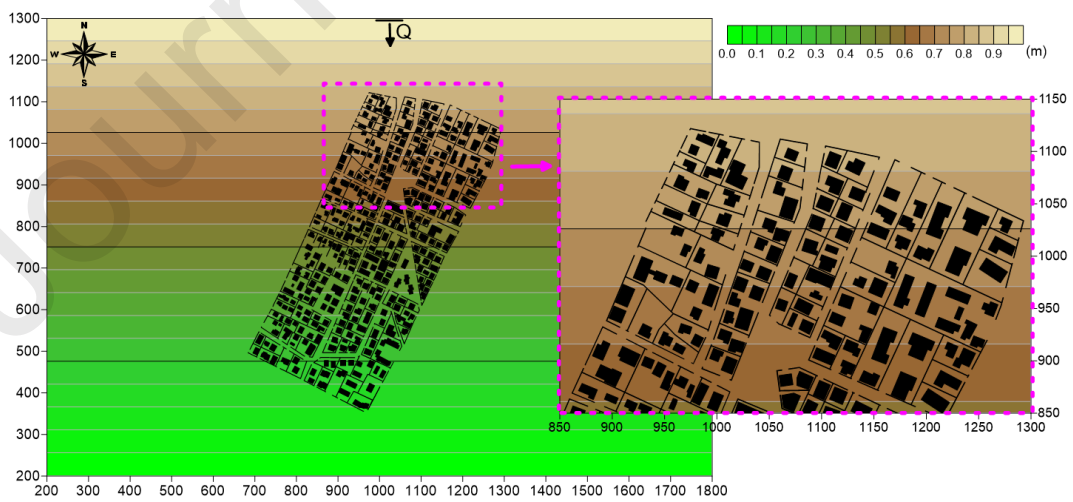
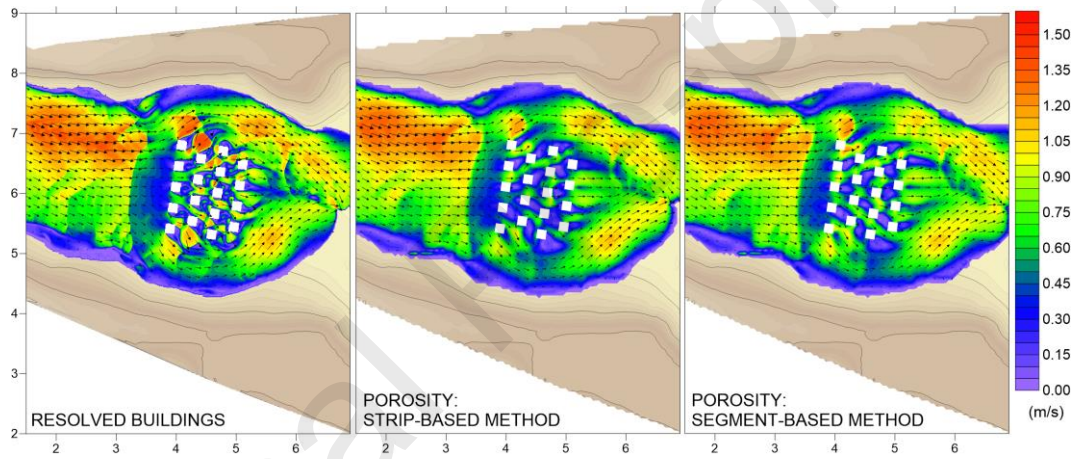
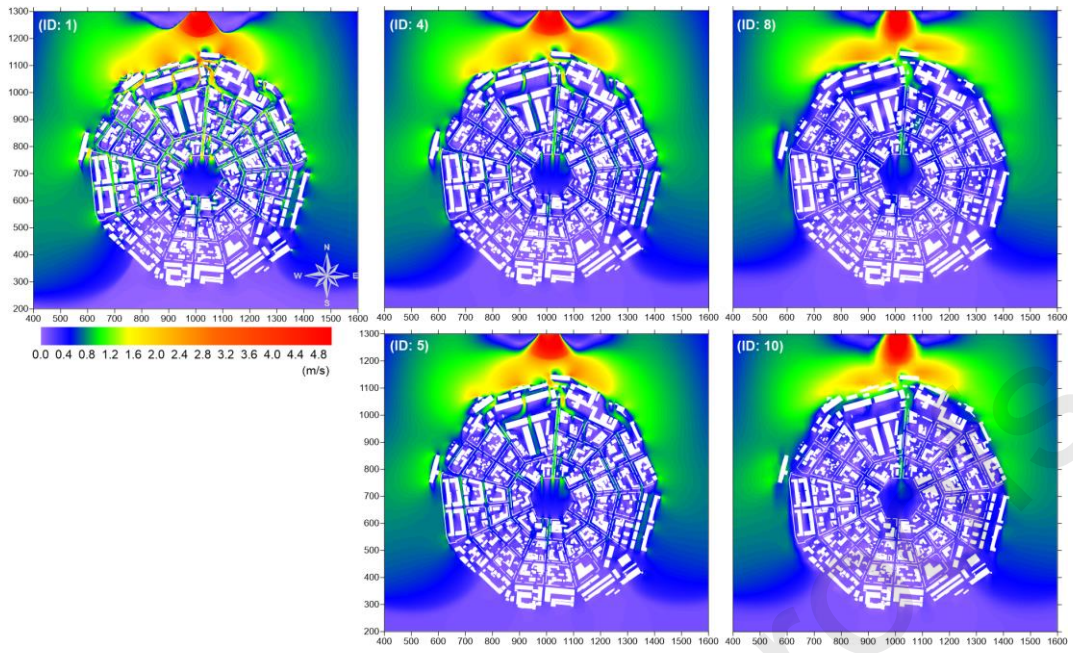


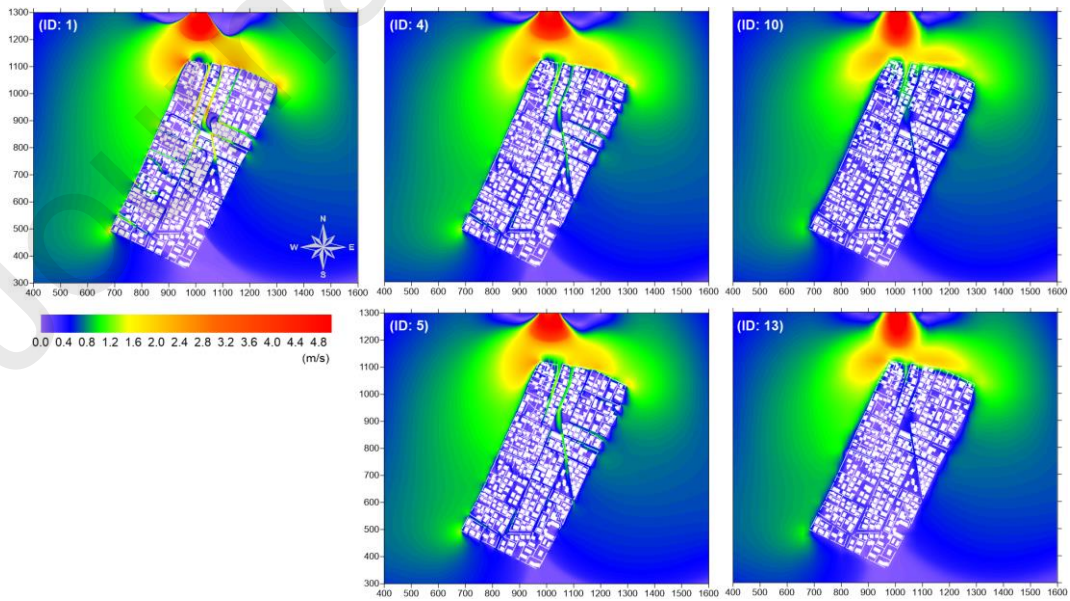
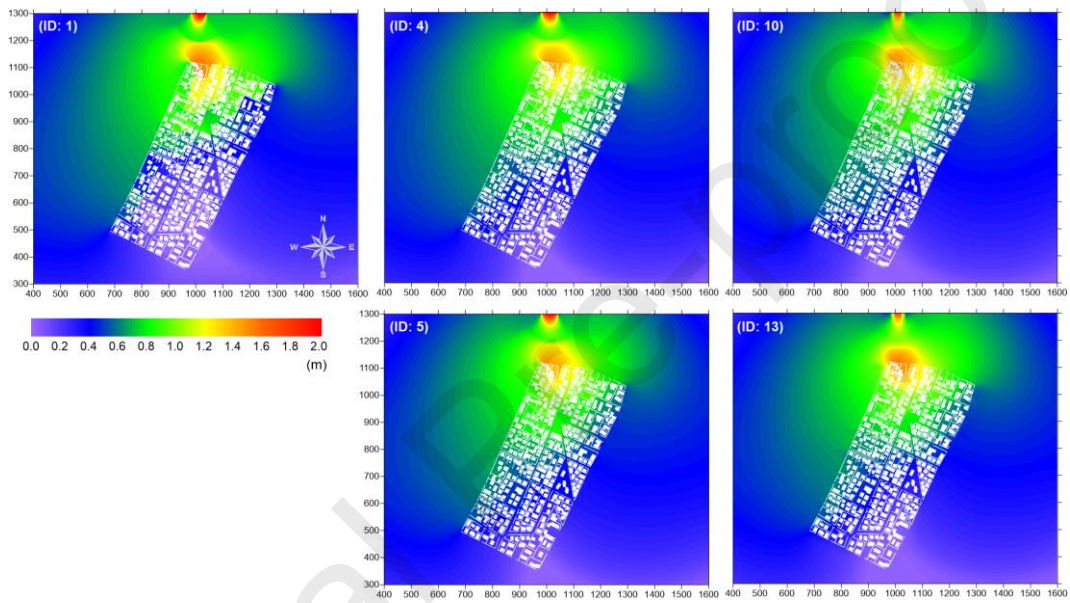
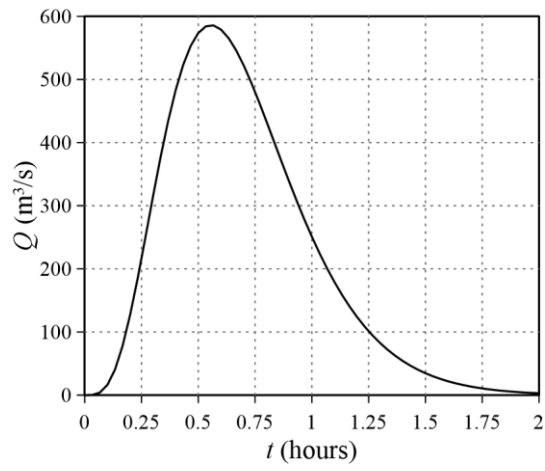












**Declaration of interests**

The authors declare that they have no known competing financial interests or personal relationships that could have appeared to influence the work reported in this paper.

The authors declare the following financial interests/personal relationships which may be considered as potential competing interests:

The Authors equally contributed to this work.

### **Abstract**

In the framework of porosity models for large-scale urban floods, this work presents a method to compute the spatial distribution of the porosity parameters of complex urban areas by analyzing the footprints of buildings and obstacles. Precisely, an algorithm is described that estimates the four parameters required by the differential, dual-porosity formulation recently presented by Viero (2019) [J. Hydrol. 568, 247-259] and by Ferrari et al. (2019) [Adv. Water Resour. 125, 98-113]; in this formulation, beside the common isotropic porosity accounting for the reduced storage volume due to buildings, a cell-based conveyance porosity is introduced in the momentum equations in tensor form to model anisotropic resistances and alterations in the flow direction due to presence of preferential pathways such as streets. A cell-averaged description of the spatial connectivity in the urban medium and of the preferential flow directions is the main ingredient for robust and mesh-independent estimates. To achieve this goal, the algorithm here presented automatically extracts the spatially distributed porosity fields of urban layouts relying only on geometrical information, thus avoiding additional calibration effort. The proposed method is described with the aid of schematic applications and then tested by simulating the flooding of real, complex urban areas using structured Cartesian grids. A Fortran implementation of the algorithm is made available for free download and use.

Journal Pre-proofs